









RESEARCH ARTICLE OPEN ACCESS

Full-Scale Beam-To-Column Subassembly Testing for Seismic Evaluation of Deep Columns

Claudio Sepulveda^{1,2}  | Gulen Ozkula³  | Gilberto Mosqueda¹  | Chia-Ming Uang¹  | Chung-Che Chou^{4,5}  | Kung-Juin Wang⁴  | Sherif El-Tawil⁶  | Jason McCormick⁶ 

¹Department of Structural Engineering, University of California San Diego, La Jolla, California, USA | ²Department of Civil Engineering, Universidad Tecnica Federico Santa Maria, Valparaiso, Chile | ³Department of Civil Engineering, University of the District of Columbia, Washington, District of Columbia, USA | ⁴National Center for Research on Earthquake Engineering (NCREE), Taipei, Taiwan | ⁵Department of Civil Engineering, National Taiwan University, Taipei, Taiwan | ⁶Civil and Environmental Engineering Department, University of Michigan, Ann Arbor, Michigan, USA

Correspondence: Claudio Sepulveda (csepulve@ucsd.edu; claudio.sepulvedac@usm.cl) | Gilberto Mosqueda (gmosqueda@ucsd.edu)

Received: 20 April 2024 | **Revised:** 25 December 2024 | **Accepted:** 3 January 2025

Funding: This project was funded by NIST under Award 70NANB17ITZ91 to the University of Michigan and UC San Diego and by the National Center for Research on Earthquake Engineering (NCREE) supported by the Ministry of Science and Technology (MOST 110-2625-M-002-015), Taiwan.

Keywords: deep columns | full-scale subassembly | hybrid simulation | quasi-static | reduced beam section | steel moment frames

ABSTRACT

Steel moment frames composed of wide-flange steel members are commonly used in seismic regions, with deep and slender column sections often selected to economically satisfy drift limit requirements. The section slenderness makes the columns more susceptible to local and global buckling and subsequent axial shortening when subjected to combined high axial forces and lateral deformations. Numerous tests have been conducted on individual column members under a wide range of axial loads and loading patterns. Experimental data of subassembly or complete frame configurations providing insight into system level interaction of the column with the frame are more limited. To address this concern, a full-scale testing program was conducted on four cruciform beam-to-column subassembly subjected to loading patterns based on cyclic quasi-static and slow hybrid simulation. Quasi-static tests followed standard AISC loading protocol with constant column axial load ranging from 20% to 40% of the yield capacity. Advanced hybrid simulations subjected the specimens to realistic earthquake loading patterns to levels consistent with design basis earthquake (DBE) and maximum considered earthquake (MCE) ground motions. A full nonlinear model of a complete 6-story frame was developed for the numerical substructure in the hybrid simulation. The observed local and global responses of two quasi-static and two hybrid tests are presented, providing valuable data towards improving the understanding of progress of damage for these systems through advanced testing techniques.

1 | Introduction

Wide-flange steel column members are commonly used for steel moment frames in seismic regions. Following the 1994 Northridge Earthquake, more restrictive drift requirements for buildings [1] resulted in the use of deep columns with increased moment of inertia and stiffness with minimal sectional area. However, deep

columns are susceptible to experiencing local and global buckling that can result in axial shortening [2] and significantly degrade member resistance [3, 4]. An accurate prediction of the residual deformation including axial shortening impacts the reparability or the potential need for demolition [5]. Axial shortening may also produce a redistribution of vertical forces between adjacent columns due to the differential settlement.

This is an open access article under the terms of the [Creative Commons Attribution](https://creativecommons.org/licenses/by/4.0/) License, which permits use, distribution and reproduction in any medium, provided the original work is properly cited.

© 2025 The Author(s). *Earthquake Engineering & Structural Dynamics* published by John Wiley & Sons Ltd.

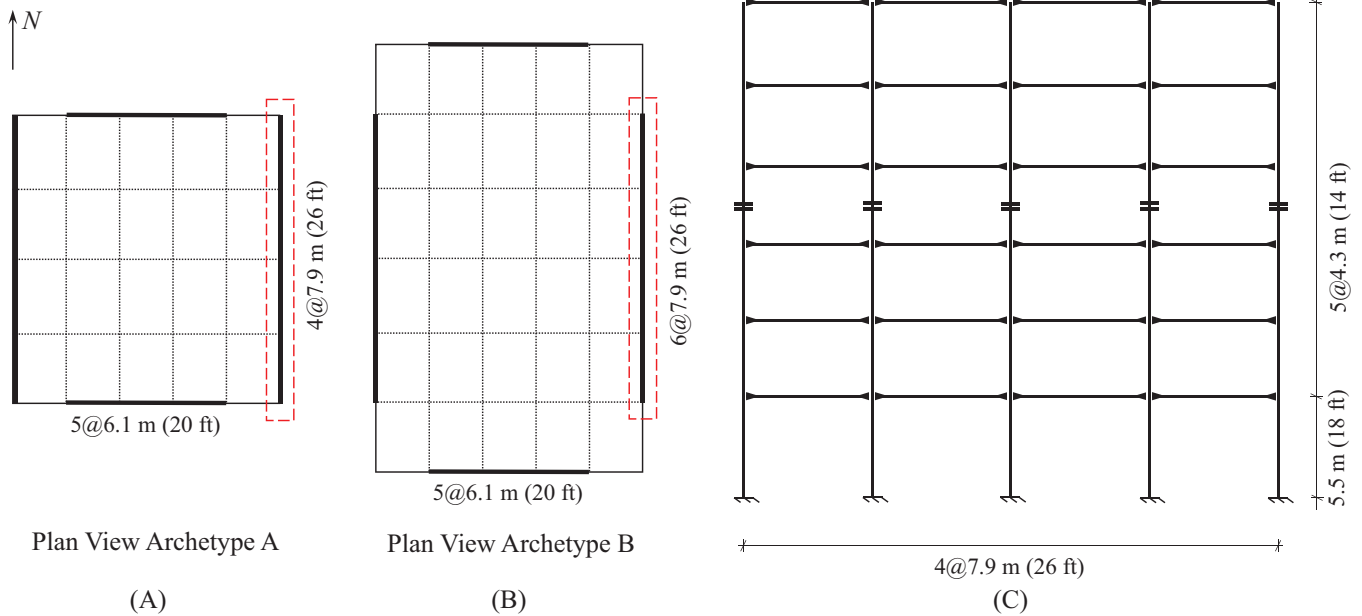


FIGURE 1 | Archetype building scheme: (A) Plan view specimen A, (B) plan view specimen B, and (C) elevation for both archetype buildings A and B.

Numerical simulations using high-fidelity finite elements models have been carried out for single wide-flange columns to characterize their stability under combined axial and lateral loads [3, 6–9]. Experiments have been conducted on isolated column members to characterize this behavior under quasi-static load patterns at various axial loads [10, 11]. Those studies have exposed the effects of the axial load magnitude and pattern, inelastic deformation, and boundary conditions on the resulting axial shortening [2, 12]. While the impact of column buckling and subsequent axial shortening has been numerically examined from a system-level point of view [13–15], there is limited experimental data for system-level verification.

A testing program was conducted to experimentally assess the system behavior of moment frame structures with deep and slender columns. Two specimens were subjected to quasi-static (QS) loading protocols and another two were subjected to more realistic seismic loads using hybrid simulation (HS). The tests were conducted on full-scale cruciform subassemblies at the National Center for Research on Earthquake Engineering (NCREE) in Taiwan. Experimental observations are presented here for the four specimens having deep and slender wide-flange columns, complementing previous work of similar tests conducted on box column [12, 16]. Quasi-static tests are first performed to assess the cyclic behavior of the subassembly following the standard AISC loading protocols for steel structures [17]. Hybrid simulations using advanced testing methods are also conducted at an extended time scale (not real-time) to quantify the structural damage of the frame structure directly under simulated seismic loads using historical ground motion records. The hybrid simulations include a full nonlinear numerical model of the prototype frame and applies a novel mixed displacement and force control method [18] along with an online model updating scheme [19].

TABLE 1 | Summary of member section.

Archetypes:	Building A	Building B
Column section (1st to 3rd floor)	W24 × 131	W24 × 176
Beam section (1st to 3rd floor)	W27 × 94	W27 × 129
Column section (4th to roof floor)	W24 × 117	W24 × 131
Beam section (4th to roof floor)	W27 × 84	W27 × 94
1st story column $\lambda_f = b_f/2t_f$	6.7	4.81
1st story column $\lambda_w = h/t_w$	35.6	28.7

2 | Archetype Structures

Two six-story archetype steel moment frame (SMF) structures were designed to investigate the seismic performance of first-story column with varying slenderness ratios. The building plan view and elevation are depicted in Figure 1 for both archetypes. The structural system is designed for both vertical and lateral loads following provisions outlined in ASCE 7–16 [1] and AISC 341–16 [20] for a site located in San Diego, California, with soil type D ($S_{DS} = 0.995$ g, $S_{D1} = 0.503$ g). The first story height is 5.5 m (18 ft), while all other stories have 4.3 m (14 ft) in height. The seismic-resistant frame in the north-south (N-S) direction examined in this study is comprised of four bays, each measuring 7.9 m (26 ft) in length.

The use of W24 × 176 and W24 × 131 sections for the first-story columns with a height of 5.5 m is specifically chosen to facilitate comparisons with the results of member-level tests conducted by Chansuk et al. [11]. The columns were classified as slender based on the slenderness ratios for the flange ($b_f/2t_f$) and web (h/t_w) and their proximity to the seismic compactness limits for

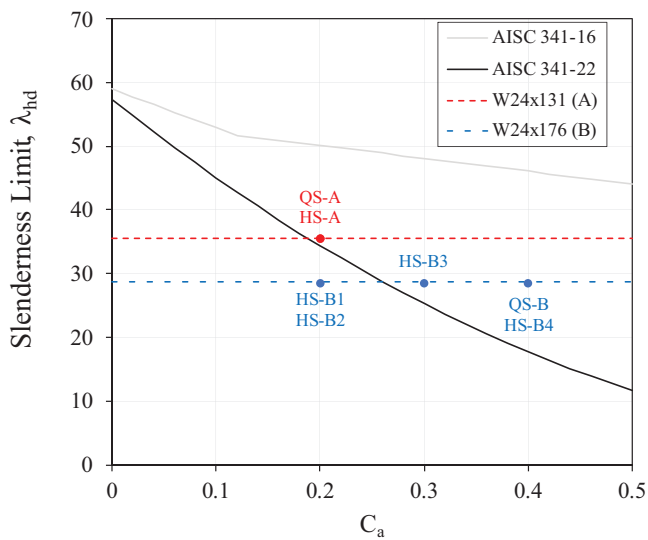


FIGURE 2 | AISC web slenderness requirements for highly ductile members and columns tested.

highly ductile members as per AISC 341-16 [20], the design code in use at the time of the design of the archetypes. Table 1 shows beam and column cross sections and column slenderness. The structural steel components are constructed using A992 steel. Figure 2 illustrates the web slenderness requirements for highly ductile members per AISC 341-16 [20]. The limit required by AISC 341-22 [21] is also indicated for reference, although it was released after the test specimens were designed. It is important to note that in the 2016 edition, all selected columns for archetype buildings were classified as highly ductile members. However, in the 2022 edition, this classification has been revised due to the increased emphasis on axial load considerations. The dead load for the design was 4.1 KPa (85 psf) and 3.8 KPa (80 psf) for the first five floors and roof, respectively, while the reduced live load was 0.5 KPa (10 psf) for all stories. Based on past studies and experience, first-story columns are typically subjected to axial forces ranging from 5% to 20% of their yield capacity [4]. The design of the archetype building considered here resulted in the gravity forces of interior columns equivalent to $C_a = 8.5\%$ and 6.5% , for archetypes A and B, respectively. However, overturning effect can add up to $C_a = \pm 23\%$ according to numerical simulations of these archetypes. For the purpose of this experimental program, first-story columns were subjected to an axial force ranging from 20% to 40% of their yield capacity to investigate typical and beyond design cases. This range of loading also allows for a direct comparison with member-level test of columns with similar sections [4, 11].

In the building design, the SMF columns were assumed to be fixed at their base and spliced at the mid-height of the fourth story. An initial estimate of the fundamental period for both steel moment frame archetypes was 1.4 s, as determined using ASCE 7-16 [1]. The beam-column connection considers a doubler plate for the panel zone, continuity plates, and reduced beam sections (RBS) per the guidelines provided by AISC 341-16 [20] and AISC 358-16 [22]. The steel backing between the beam top flange and the column was not removed, and a reinforcing fillet weld was added below the steel backing. The steel backing between the bottom beam flange and the column was removed,

and the root pass was back gouged to sound weld metal and back welded with a reinforcing fillet. Bolts in the beam web were used for erection purposes, and a CJP groove weld was provided between the entire height of the beam web and the column flange. Before testing, all CJP groove welds passed the ultrasonic test (UT) inspection. The column was connected to the concrete strong floor of the lab through a 60 mm thick base plate and 36 posttensioned steel rods. Figure 3 shows details of the beam-to-column connection and the base plate for archetypes A and B.

3 | Experimental Program

3.1 | Subassembly Description

To study the story-level behavior and the interactions between columns, beams, and beam-to-column connections, a cruciform subassembly was selected for the experimental program. The specimen height is one and one-half stories, including beams on each side extending half the bay length. External transducers located at the bottom of the panel zone are assigned as the control point for the system loading. The lateral displacement of the specimen is applied by two pin-connected actuators located at the top of the subassembly commanded to match the displacement feedback of the control point. The axial force was applied by four hydraulic jacks on a loading beam attached to the top of the column and anchored to the strong floor through steel rods. Pin-connected vertical actuators control the vertical displacement of each beam end, following the vertical movements of the control point below the panel zone including axial shortening of the column, if occurs. This assumes that any vertical displacement experienced by the column during quasi-static or hybrid tests is similar in neighboring columns and maintains the presumed point of inflection for the beam at the same height. The cruciform subassembly and the actuator configuration are illustrated in Figure 4A.

3.2 | Experimental Setup

The experimental setup required lateral restraints to maintain the in-plane response of the frame. Column flanges at the panel zone and beam top flanges were laterally braced using lubricated horizontal plates supported by diagonal bracing (blue bracing elements of Figure 4B) to replicate the bracing provided by the slab. Beams were also braced along the length with additional lateral supports.

The instrumentation layout is depicted in Figure 5. The *Opti-track Motion Capture Systems* (MoCap) was utilized to track the absolute displacement of the specimen. LED sensors (not shown) were installed throughout the specimen with a clear line of sight such as the column to enable monitoring of the 3D movement. Strain gauges were utilized along the specimen to capture the beams and column flange response. Inclinometers monitored the absolute rotation at different locations. To better visualize damage in regions of interest, a 10 cm grid was drawn in the column base and RBS zone. Two orthogonal Tempsonic linear position sensors (Tempsonic III) measured the in-plane displacement of the control point with a resolution of 0.005 mm.

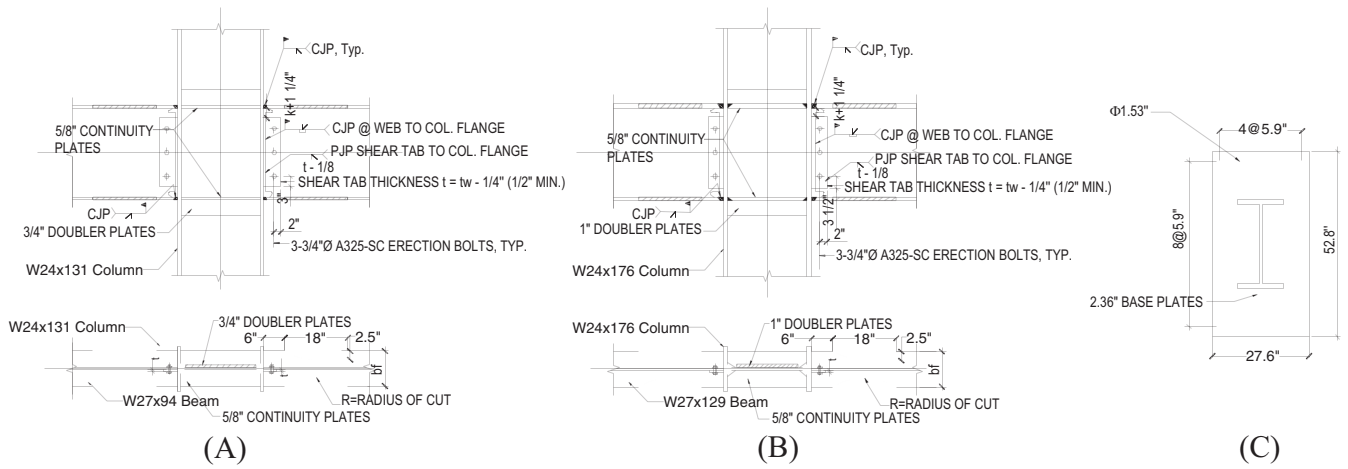


FIGURE 3 | Connection details: (A) Beam-to-column for archetype A, (B) beam-to-column for archetype B, and (C) base plate for both archetypes.

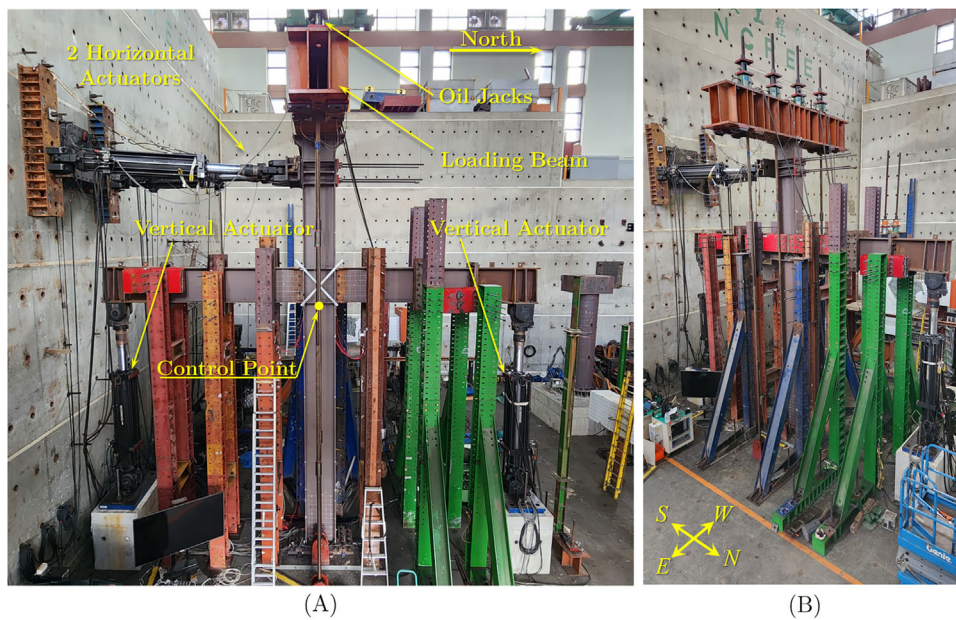


FIGURE 4 | Experimental setup showing: (A) Specimen and actuator configuration and (B) lateral bracing.

Horizontal and vertical displacement components are computed within MTS controller applying kinematic transformations to control the horizontal and vertical actuators. High-sensitivity displacement transducers were employed to monitor the rotation and sliding movement of the column base plate (see Figure 6A). Two similar devices were also used to compute the rotation across the RBS as shown in Figure 6B for the online model updating application. The shear distortion of the panel zone is calculated based on the measurement from an X-shape instrument configuration using Pi-shape displacement transducer (see Figure 6C).

3.3 | Test Matrix

Four specimens were tested: two using archetype Building A and two using archetype Building B. A quasi-static test and a hybrid simulation were conducted on each archetype. Table 2 summa-

rizes the test matrix, including the sequence and designation of Test ID for each test. Figure A1 in the Appendix shows the response spectrum of each ground motion. The column axial load for quasi-static tests was constant and based on C_a defined as the “ratio of required strength to available axial yield strength” per AISC-341-22 [21]:

$$C_a = \frac{\alpha_s P_r}{R_y F_y A_g} \tag{1}$$

where $\alpha_s = 1$ is force level adjustment factor for LFRD design, F_y the nominal yield strength, and $R_y = 1.1$ for A992 steel. For the hybrid tests, the axial load is obtained from the numerical model and is not constant due to redistribution of axial forces between columns caused by shortening. The column axial force shown in the table for HS corresponds to the gravity load at the start of the seismic excitation. The drifts listed are the maximum achieved for each test.

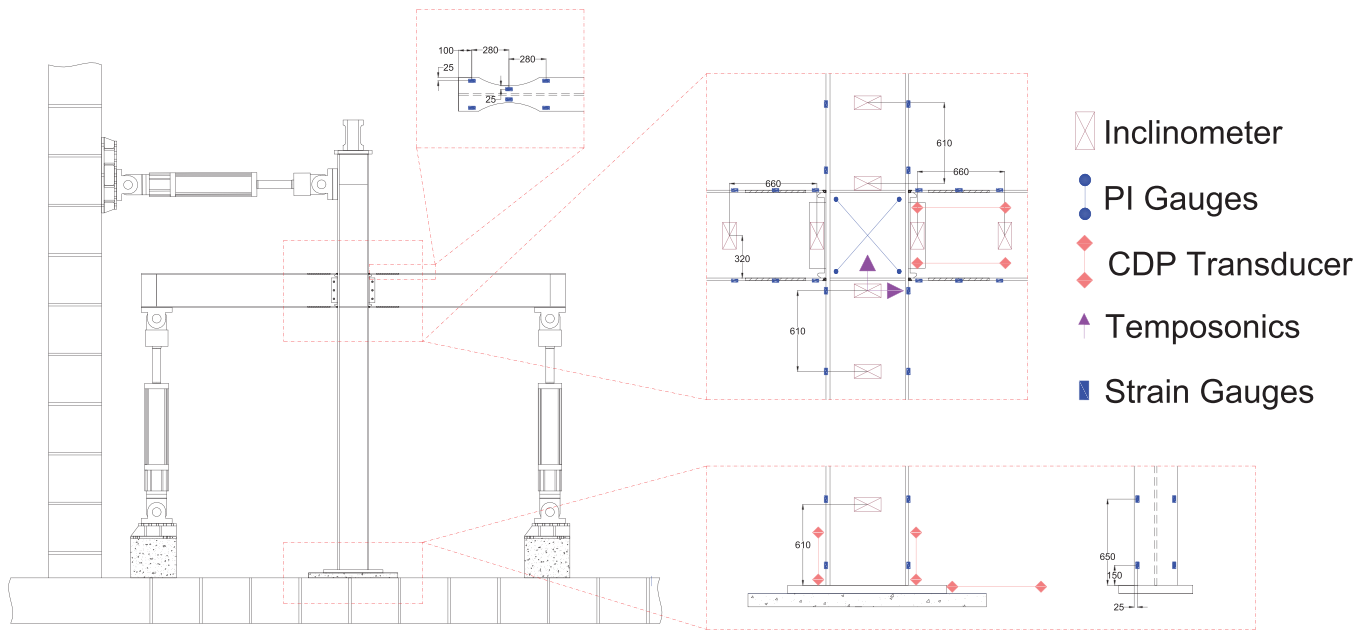


FIGURE 5 | Instrumentation setup.

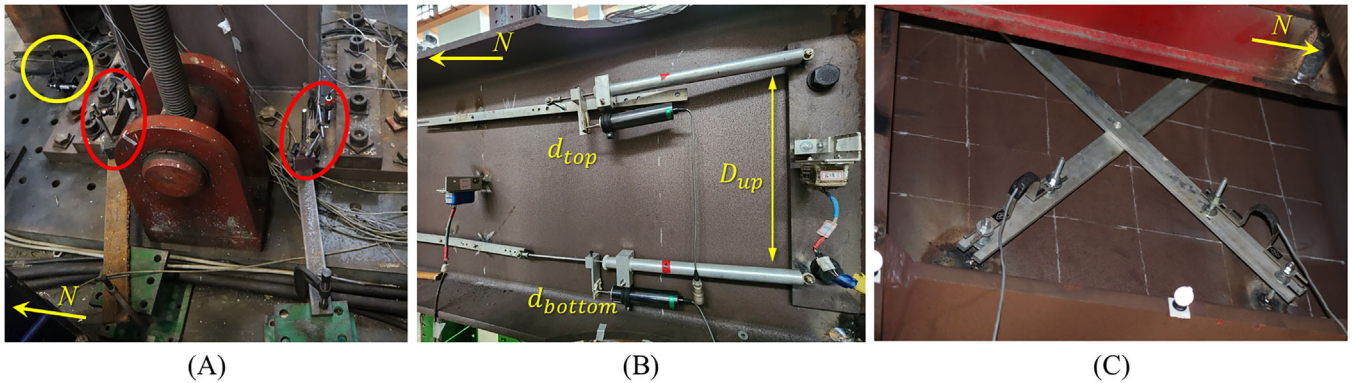


FIGURE 6 | Displacement transducer setup for local measurements of: (A) base plate overturning (red) and sliding (yellow); (B) RBS rotation; and (C) panel zone shear distortion.

TABLE 2 | Summary of test matrix.

Test ID	Type of test	Arch.	Axial force		Ground motion for HS		Drift (%)	
			C_a (%)	(kN)	Level	Earthquake	(-)	(+)
QS-A	Quasi-static	A	20	1885	—	—	-3.3	4.3
HS-A1	Hybrid simulation	A	20	1885	Elastic	Kobe (1995)	-0.14	0.15
HS-A2	Hybrid simulation	A	20	1885	DBE+MCE	Kobe (1995)+Chi-Chi (1999)	-2.9	2.5
HS-A3	Hybrid simulation	A	20	1885	MCE	Northridge (1994)	-2.9	2.0
HS-A4	Hybrid simulation	A	20	1885	1.3MCE	Northridge (1994)	-2.7	2.4
QS-B	Quasi-static	B	40	5063	—	—	-3.0	3.0
HS-B1	Hybrid simulation	B	20	2532	Elastic	Kobe (1995)	-0.15	0.14
HS-B2	Hybrid simulation	B	20	2532	DBE+MCE	Kobe (1995)+Northridge (1994)	-5.0	1.5
HS-B3	Hybrid simulation	B	30	3797	1.3MCE	Kobe (1995)	-3.1	3.3
HS-B4	Hybrid simulation	B	40	5063	1.3MCE	Kobe (1995)	-2.9	2.5

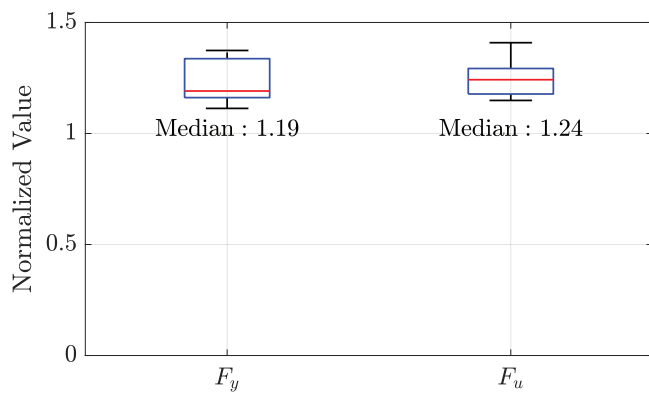


FIGURE 7 | Box and whisker plot of normalized properties measured from tensile coupon tests.

Each test configuration is also compared against the AISC slenderness requirements for highly ductile members of 2016 and 2022 editions, as shown in Figure 2. Material tensile testing was conducted for each specimen using coupons extracted after subassembly tests were completed. Figure 7 presents a box and whiskers plot of the measured properties normalized by the corresponding nominal value of $F_y = 345$ MPa and $F_u = 450$ MPa. Table A1 in the Appendix provides details of the measured properties.

The symmetric protocol specified by AISC-341-22 [21] was applied for quasi-static tests up to a 5% drift ratio, which was the maximum displacement allowed by the test setup. However, none of the quasi-static tests reached 5% drift since significant damage was observed before such drift.

Four hybrid tests were conducted for each selected specimen using different intensities of ground motions as shown in Table 2. The testing plan consisted of first conducting a low-level test to check all the instrumentation and hardware/software connectivity while maintaining the specimen in the linear-elastic range. Then, a sequence of a DBE followed by an MCE ground motion was preprogrammed to account for the cumulative damage and residuals within the numerical and experimental substructure. Following this sequence, both specimens remained with sufficient capacity and additional HS were conducted to obtain more experimental data on cumulative damage. For those tests, the simulation had to be reset, and did not maintain the residual state of the numerical substructure.

4 | Hybrid Simulation Setup

4.1 | Numerical Substructure

The hybrid simulation comprised the complete 5-bay 6-story frame and associated weight and mass. The numerical model was developed utilizing the OpenSees platform [23]. Columns were assumed to have fixed connections at the base and were represented using distributed plasticity elements employing a displacement-based formulation with four Gauss-Lobatto points. The change in sectional properties due to column splices were considered by using different sections for the upper and lower portion. The panel zone flexibility was simulated using the

parallelogram approach with a rotational spring in one of the corners [24].

Beams were modeled using an elastic beam-column element for the middle section, with rigid offsets and a lumped plasticity rotational spring at each end. Starting from the third-floor and above, the response of the RBS was simulated using the Ibarra-Medina-Krawinkler (IMK) model [25], with properties initially defined based on the recommendations of Lignos and Krawinkler [26], and then adjusted based on the quasi-static results. For the RBS hinges located on the second-floor, a Bouc-Wen model was used as part of the Online Model Updating (OMU) scheme that updated the numerical hinge properties based on the measured data during the HS. More details about OMU can be found in Sepulveda et al. [19]. Rayleigh damping assigned as 2.5% of critical was added as inherent damping anchored to the first and third vibration modes. A P-Delta transformation was incorporated into column elements. A leaning column was added alongside the moment frame to account for the contribution of the gravity frame. The natural period obtained from the numerical models are 1.53 and 1.58 s for archetypes A and B, respectively.

4.2 | Substructuring and Control Strategy

Numerical simulations conducted on the complete frame showed negligible differences in loads and deformations among the three interior columns [27]. Considering the cruciform subassembly and test setup, the physical substructure was defined to represent the behavior of the three interior first-story columns, while the exterior columns were simulated in the numerical substructure. Although the exterior columns may also experience axial shortening due to buckling, previous isolated column testing has demonstrated that the axial load variation resulting from overturning delays local buckling initiation and significantly reduces axial shortening when compared to interior columns with more constant loading [4]. In these simulations, the axial shortening of the exterior columns was solely attributed to material nonlinearity through the fiber-based column element.

The experimental subassembly had hinge connections at the ends of beam and columns following typical practice of assuming inflection points at the midspan of beams and midweight of the column. To better account for these boundary conditions in the hybrid simulation, an overlapping substructuring method [28] was applied. A diagram of the substructuring approach together with the hybrid loop and online model updating loop are exhibited in Figure 8, noting the overlap between the experimental second story and the numerical substructure. The two paired horizontal actuators on top of the subassembly applied the horizontal displacement at the control point as commanded by the numerical model. The axial load command computed by the numerical substructure was applied using the force-controlled oil jacks on top of the specimen. The two vertical actuators maintained the end of the beams at the same vertical position of the panel zone following any shortening including that due to buckling of the column. Further details regarding the control strategy can be found in Sepulveda et al. [18].

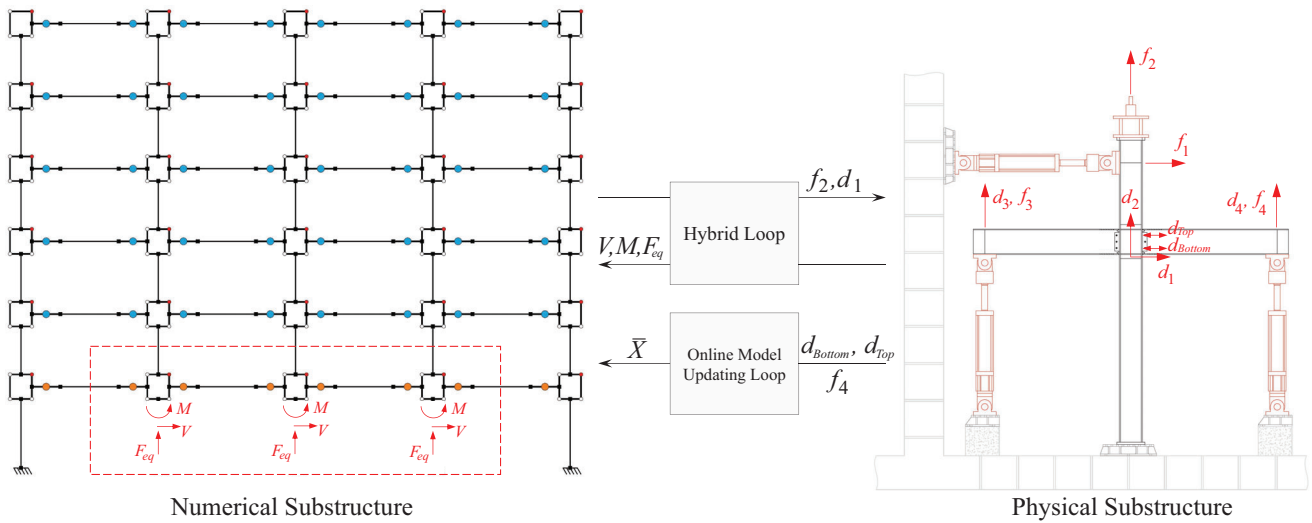


FIGURE 8 | Substructuring scheme.

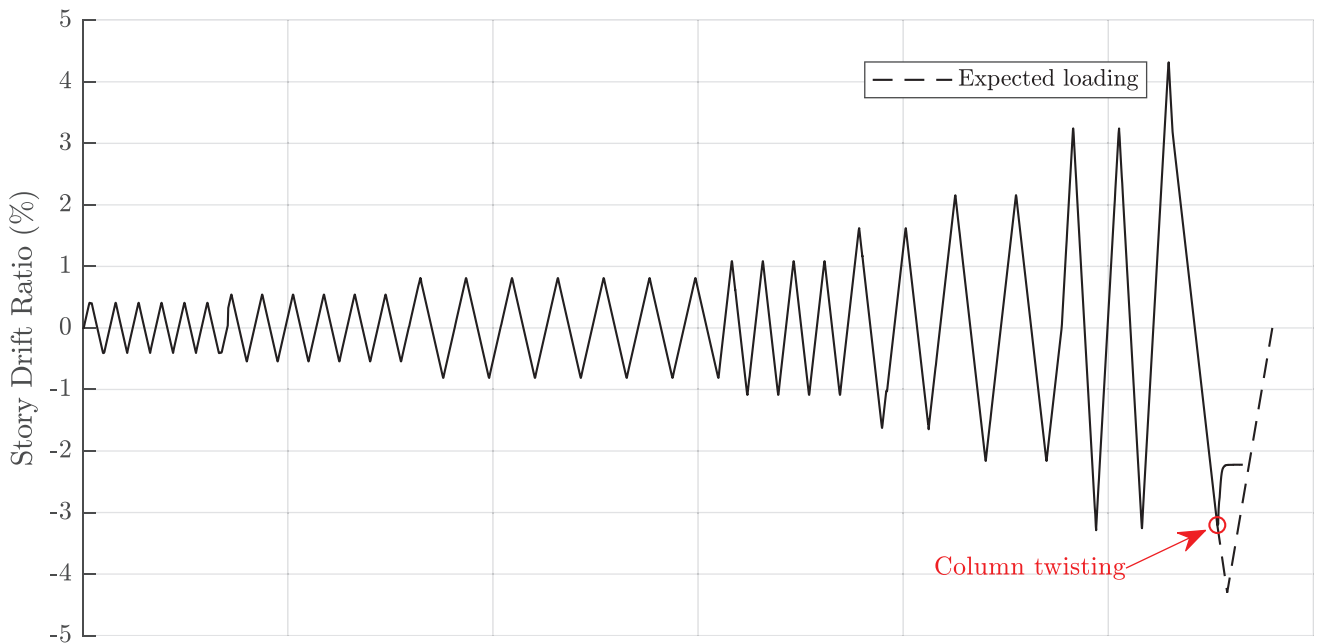


FIGURE 9 | Loading protocol for QS-A test.

5 | Experimental Results: Specimen A

5.1 | Test QS-A

Conducting the experimental program at this scale and size came with significant challenges in terms of the setup and fully restraining out of plane motion. The setup was first developed for similar specimens with box columns having large out-of-plane stiffness [16]. Accounting for the column slenderness in the weak axis, it was difficult to apply direct restraints at the top of specimen considering the elevation, scale and location of the setup. Two horizontal actuators were initially placed in a V-shape configuration to control the out-of-plane displacement of the specimen at the top for this research. After the first cycle of +4.3% drift, the severity of both the column and RBS local buckling increased, producing column twisting. The testing was stopped before the first peak at -4.3% due to excessive specimen

twisting. Figure 9 depicts the drift ratio measured during the test. For the following tests, the out-of-plane deformation was successfully controlled by reinforcing the lateral bracing at the beam elevation, and the column twisting was controlled through a parallel configuration for the horizontal actuators, both working in displacement control mode. The torsional constraint was necessary for laboratory safety. It should also be noted that in the quasi-static test of specimen A, the applied drift ratio slightly exceeds AISC 360-16 values because the control point was positioned below the reference height for the actuator-imposed deformation. This was corrected for the following tests.

5.2 | Test HS-A

The experimental substructure was replaced with an identical Specimen A and subjected to four consecutive hybrid simulations.

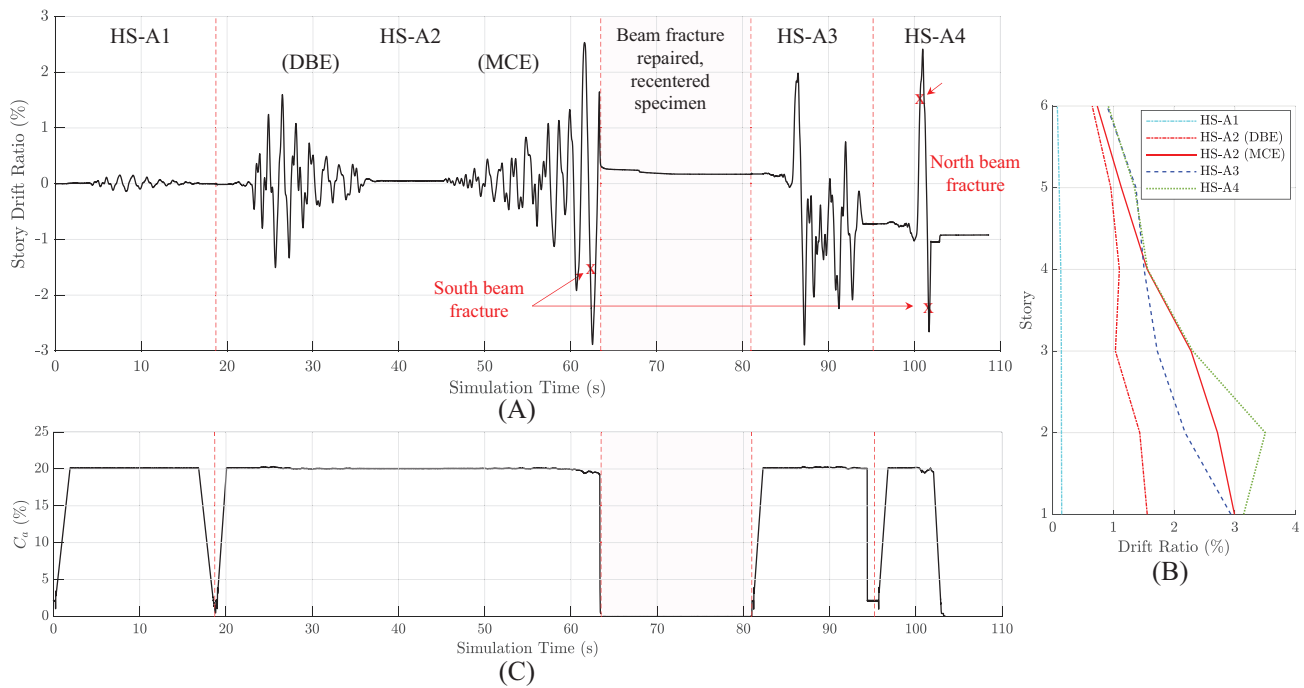


FIGURE 10 | Response from HS-A tests: (A) First story drift; (B) maximum story drift (numerical substructure); and (C) axial load history.

HS-A1 was an elastic level simulation used to verify the test setup and control algorithm. HS-A2 was composed of a sequence of DBE and MCE ground motions. The test was stopped prior to reaching the maximum response of the MCE motion due to a fracture of the bottom flange weld of the south beam and excessive tilting of the loading beam on top of the specimen. The fracture was repaired, and the specimen was recentered to minimize residual deformations and forces on the specimen and the beam. The testing was continued with HS-3 using a different MCE level motion in order to further evaluate the column behavior. An additional test HS-A4 was conducted to evaluate the remaining capacity of the specimen. The numerical substructure was restarted for this test, losing the residual state of the numerical model and actuator forces were manually brought to zero maintaining the horizontal offset. The ground motion was scaled up to 1.3 times MCE to maximize the specimen drift. The test was stopped before reaching the maximum response because (i) there was notable out-of-plate rotation at the top of the column including the loading beam, (ii) both beams experienced weld fracture at the bottom flanges, (iii) and the column yielded and twisted but showed no significant buckling. The applied drift ratio history for the first story, maximum drift for all the stories, and applied axial load history can be observed in Figure 10.

5.3 | Column Response

The column response in terms of moment at the base versus first-story drift is shown in Figure 11 for both the QS and HS tests. The column showed essentially linear behavior up to 2.2% drift ratio in the QS-A test. At the first cycle of 3.25% drift, column web buckling was identified by visual inspection (Figure 12A). Antisymmetric local buckling (ALB) was noticed for the following cycles [2]. The severity of buckling increased rapidly during the 3.25% cycles, showing strength degradation in

the moment-drift response (Figure 11A). The column exhibited a 24.4% strength reduction at a drift ratio of 4.3%. Note that according to AISC 341-16 [20] the specimen of QS-A qualifies as highly ductile member by a wide margin, while it narrowly misses the requirements of AISC 341-22 [21] (see Figure 2). Therefore, the observed damage is more consistent with the requirements of the latter code. The final state of the column after one cycle at 4.3% drift is shown in Figure 12B,C.

During the hybrid tests, the severity of the damage was limited compared to the quasi-static tests. Although the maximum drift ratio achieved in the HS was only slightly smaller, no degradation was observed in the moment response, for drift ratios up to 3% (Figure 11B). Limited column web buckling was observed only at the end of the last HS, as illustrated in Figure 13A. However, despite the reinforced lateral bracing, the second story of the column twisted with RBS buckling (Figure 13B). Note that the AISC loading protocol used for QS test was originally developed for qualification test of beam-to-column connections in steel moment frames. This loading protocol was meant to be “reasonable and generally conservative,” with the total number of damaging cycles in the loading sequence representative on average, but the cumulative deformation range is conservative [29]. The more severe column buckling observed from the QS test is thus expected.

The behavior of the column is further evaluated through strain gauge measurements. Figure 14 shows the strain measurement at an elevation of 650 mm from the base plate normalized by the average measured yield strain obtained from coupon testing (see Table A1) and including the effect of the axial load. Strains measured on the two tips of a flange are displayed on the X and Y axes, respectively. If the column deforms symmetrically, the strains are equal and align at 45°. A deviation from the 45° line could indicate unsymmetrical deformations caused by

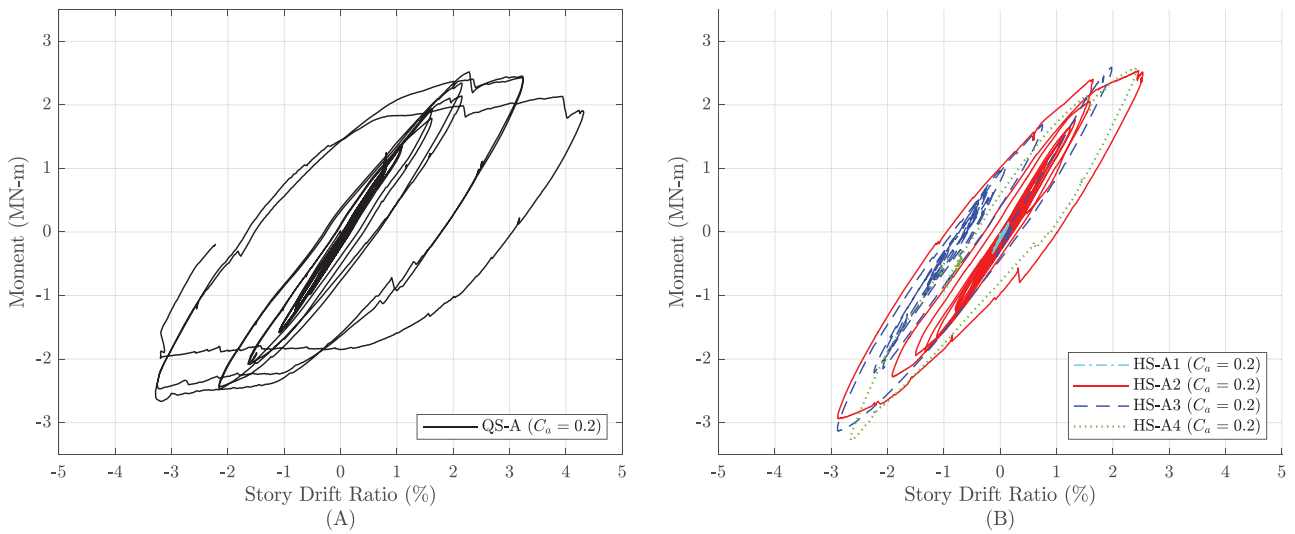


FIGURE 11 | Column base moment versus drift ratio: (A) QS-A and (B) HS-A.

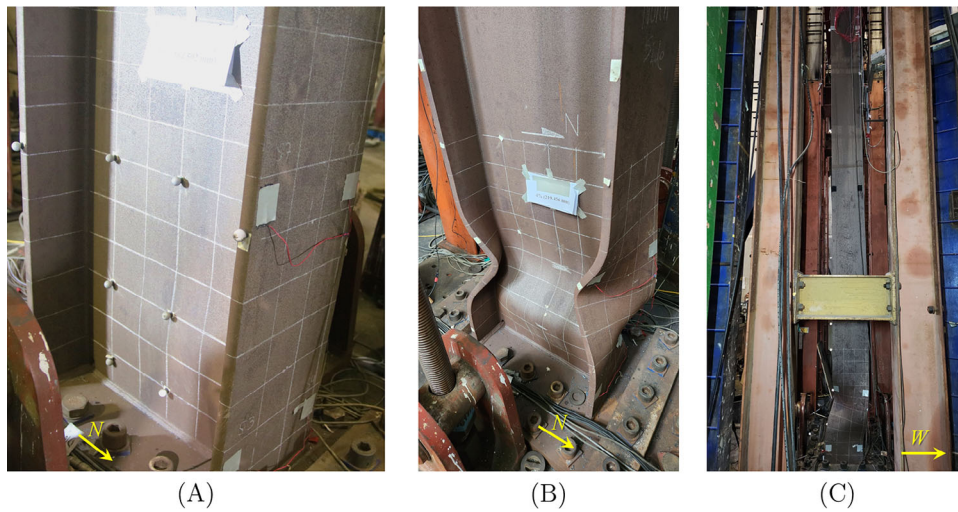


FIGURE 12 | Photos of column base for QS-A: (A) At first 3.25% drift; (B) at 4.3% drift; and (C) at 4.3% drift (lateral view).

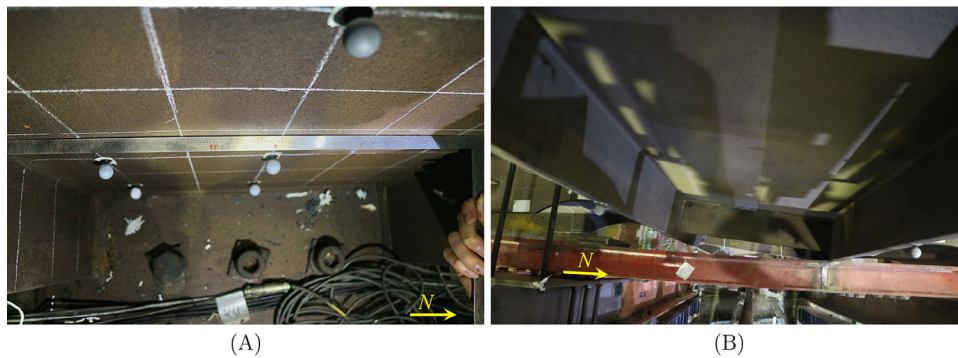


FIGURE 13 | Column state at the end of HS-A4: (A) Column base and (B) second story twisting.

buckling. As can be seen, for QS-A (Figure 14A), there is a nonsymmetric pattern after reaching 3.25% drift, in agreement with previous observations. For the hybrid tests (Figure 14B), the pattern deviates from the 45° line but remains bounded, likely due to steel yielding without buckling. More symmetric deformations

could also result from the lateral bracing improvement applied after QS-A to limit column twisting.

Axial shortening (Δ_{axial}) was monitored during all tests using the measurement at the control point. The measured values for both

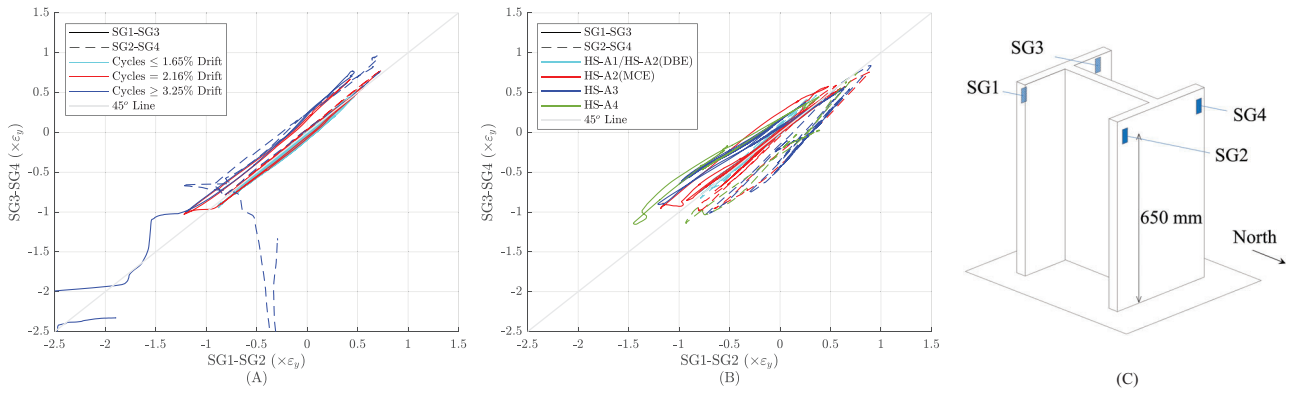


FIGURE 14 | Column flange strains: (A) QS-A; (B) HS-A; and (C) strain gauge location.

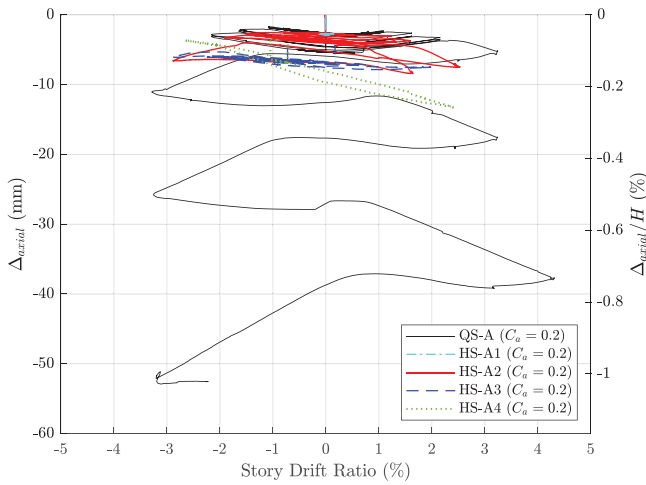


FIGURE 15 | Axial shortening versus column drift ratio for QS-A and HS-A.

QS-A and HS-A are plotted in Figure 15 as a function of drift. The value of Δ_{axial} normalized by the control point height, H , is shown at the right axis. The gravity load resulted in Δ_{axial} of around 2.5 mm. For QS-A the specimen experienced additional 2.5 mm in the last drift cycle of 2.16%. As the test progressed, column buckling became evident and Δ_{axial} continued to increase to around 26 mm by the last cycle of 3.25%, and 53 mm by the end of the test.

For the hybrid test, gravity loads resulted in a similar $\Delta_{axial} = 2.5$ mm, followed by an additional 2.0 mm after the DBE ground motion level of HS-A2 that applied peaks of $-1.9\%/1.6\%$ drift. Under the MCE ground motion, the specimen was subjected to drift ratios as large as $-2.9\%/2.5\%$, and experienced a total $\Delta_{axial} = 8.4$ mm. In the subsequent tests HS-A3 and HS-A4, vertical oscillations were observed to be correlated with the horizontal deformation of the specimen. This behavior is likely attributable to the out-of-plane tilting of the loading beam, which may have affected the displacement measurements at the control point. Notably, these last tests did not lead to substantial increase in Δ_{axial} .

For both QS-A and HS-A tests, axial shortening observed up to around 2% drift can be attributed to steel yielding, as suggested by the strain profiles and visual inspections that did

not indicate column buckling [15]. After this point, the QS test induced column buckling and significant Δ_{axial} with drift ratio of 3.25% and one cycle of 4.3% drift. On the other hand, HS did not produce a substantive increment in Δ_{axial} , even up to 2.9% drift that is relatively close to the 3.25% drift achieved in QS-A. This difference can be attributed to the dependency between buckling-induced axial shortening and the cumulative damage induced to the column as suggested by previous studies [30–32].

5.4 | Beam Response

The RBS response is presented in terms of the moment at the column face versus the measured local rotation of the RBS section. The RBS rotation is computed as $\theta_{RBS} = (d_{bottom} - d_{top})/D_{up}$, where d_{bottom} and d_{top} are the measured displacement from transducers shown in Figure 6B, and D_{up} is the distance between the transducers. Figure 16 plots the north beam response for both QS and HS. There is limited strength degradation in all the tests. Unlike the column response, the RBS response exhibits more similarities when comparing quasi-static and hybrid tests. A sudden drop in the beam strength of around 40% is observed at the end of HS-A4 due to the bottom flange fracture mentioned earlier.

Strain gauges were attached at both beam flanges along the RBS zone (see Figure 17C). Figure 17A,B presents the measurements at a distance of 660 mm away from the column face for both QS-A and HS-A. Similar to the column response, the relation deviates from the 45° line at 3.3% drift during QS-A. During the MCE level ground motion of HS-A, the pattern also deviates from the 45° pattern, but remains within a limited zone.

Figure 18A,C displays beam local buckling and lateral buckling, observed at the end of QS-A. Figure 18B depicts ductile tearing at the reduced section of the south RBS. After QS-A, more cycles were imposed on this specimen to check hardware/software connections in preparation for HS-A (not shown here). During those trials, ductile tearing increased and finally led to beam fracture.

While the column behavior had differences, beam damage in HS-A was similar to that in QS-A. Buckling wave lengths were larger for QS, but with comparable moment-rotation response. Figure 19

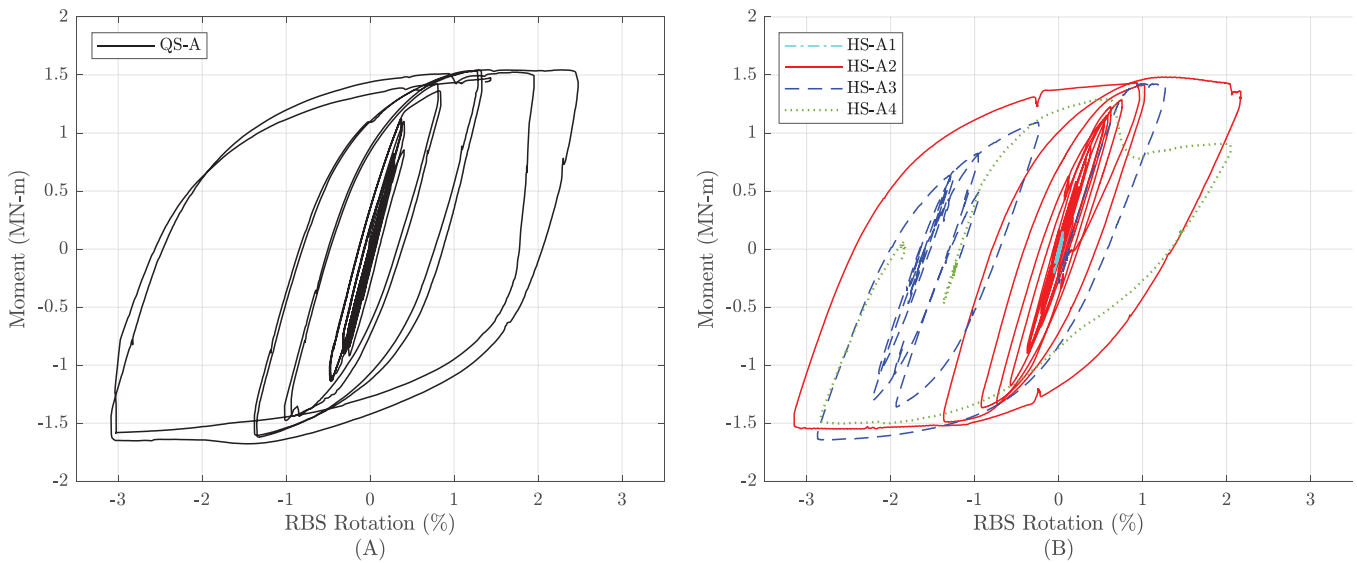


FIGURE 16 | RBS moment-rotation response: (A) QS-A and (B) HS-A.

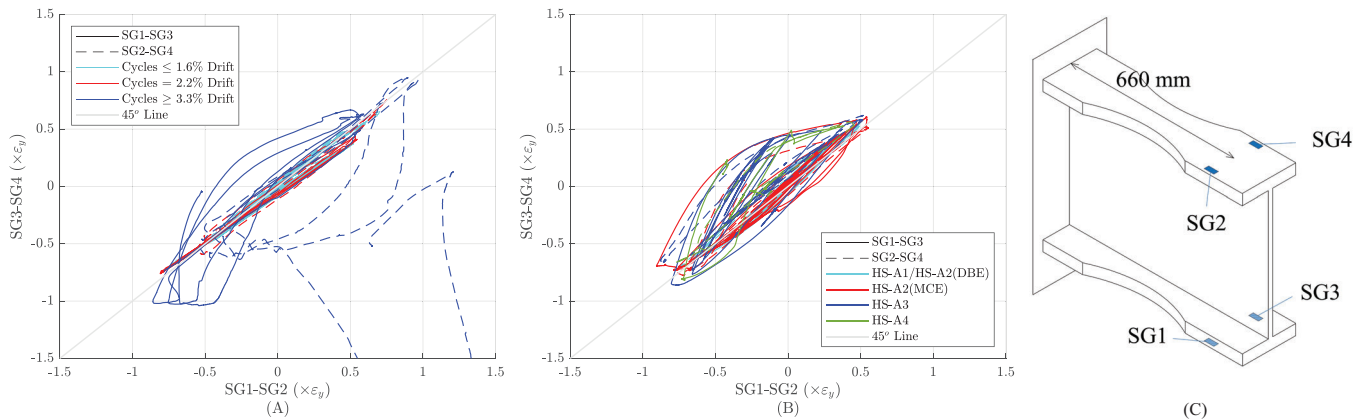


FIGURE 17 | Beam flange strains: (A) QS-A; (B) HS-A; and (C) strain gauge location.

shows the progression of beam local buckling from HS-A2 up to HS-B4. Figure 19C also shows the bottom flange weld fracture during HS-4. Lateral buckling increased its severity from HS-A2 to HS-A4 (see Figure 20).

6 | Experimental Results: Specimen B

6.1 | Test QS-B

Two specimens representative of archetype B were also subjected to a QS and HS loading sequence. Test QS-B was initially conducted using the same axial load ratio as QS-A ($C_a = 0.2$). When the specimen reached the first peak drift ratio of -2% , beam bottom flange weld unexpectedly fractured in the south beam that ended the test. With no significant damage to the column, new beams were installed using improved welding details. The loading protocol was restarted from the start and the axial load was increased to $C_a = 0.4$ to examine a more critical scenario. The column buckled globally and experienced excessive out-of-plane deformation and tilting before the specimen reached the first $+4\%$ drift target. Only the results from this

repaired specimen are presented here. Figure 21 shows the drift ratio measured during QS-B noting the deviation from the test plan.

6.2 | Test HS-B

The second specimen B was subjected to a sequence of four ground motions starting with $C_a = 0.2$, following a similar approach to HS-A. Figure 22 presents the specimen drift ratio history for the first story, maximum drift envelopes for all the stories of the numerical substructure, and applied axial load history per test. HS-B1 was a low-level test for verification of the setup. HS-B2 applied a sequence of DBE and MCE motions, resulting in a peak -5% drift that was near the physical limit of the experimental setup. After HS-B2, there was significant residual drift and the specimen was recentered to minimize displacement and force offsets, with no significant buckling in the column.

With the specimen already having significant damage, HS-B3 and HS-B4 were conducted to gain more insight and data on

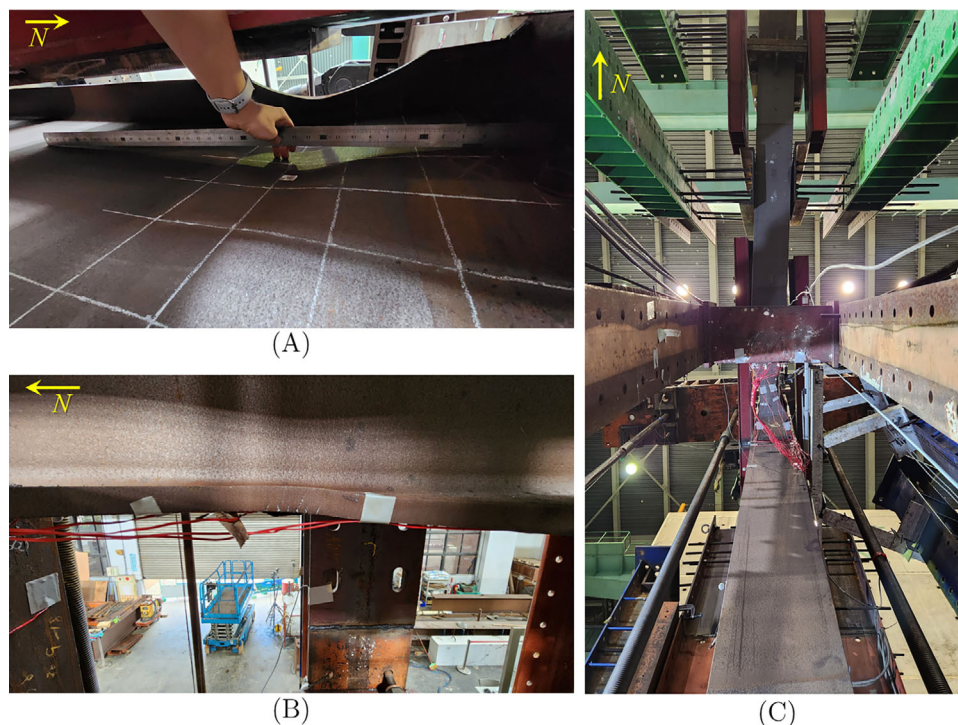


FIGURE 18 | Final state after QS-A: (A) RBS local buckling; (B) ductile tears at the south RBS; and (C) lateral buckling.

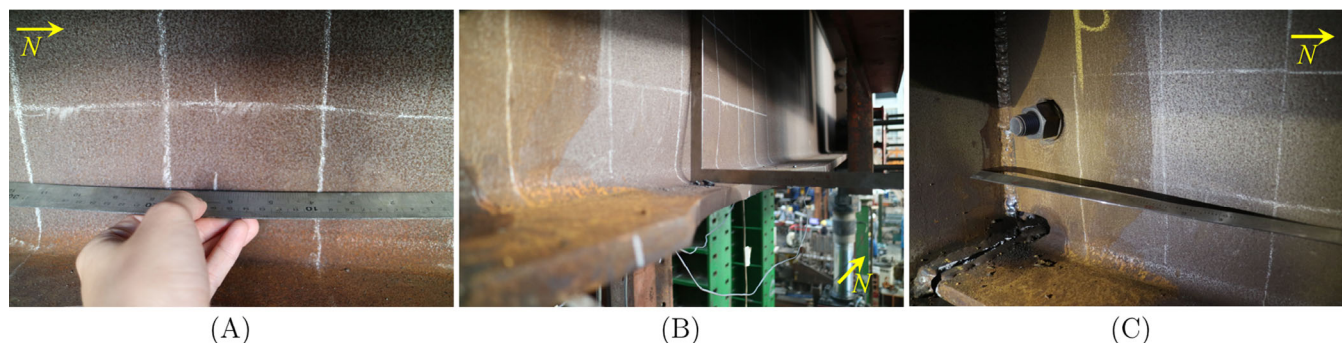


FIGURE 19 | Sequence in beam local buckling: (A) HS-A2; (B) HS-A3; and (C) HS-A4.

the residual capacity of the specimen. For HS-B3, the gravity load of the entire frame was increased to apply column axial forces equivalent to $C_a = 0.3$ for the experimental substructure. The MCE ground motion was scaled by an additional factor of 1.3 to achieve a larger positive drift in the specimen but within the setup constraints. By this stage, the column had notable web buckling at the base and ended with near-zero residual deformation. For HS-B4, the axial load was increased to $C_a = 0.4$, to induce more damage in the column while limiting drifts that can lead to increased out-of-plane movement of the specimen. The numerical substructure for archetype A was used for HS-B4 as it provided a more desirable distribution of deformations in the upper stories to better align within the limits of the test setup. By this point, the selection of the numerical model was not considered critical in terms of the expected global response since the specimen was damaged and the numerical model had to be reset and start from an undamaged state.

6.3 | Column Response

Figure 23 plots the measured response at the column base for each specimen. QS-B with $C_a = 0.4$ shows a more well-defined yield plateau and significant strength degradation especially after the first cycle at 3% drift. HS-B1 was the elastic hybrid test employed to verify hardware/software connections. HS-B2 produced a -5% drift ratio, the largest peak deformation among all the tests conducted in this study. This peak was achieved with less cycles and lower axial load compared to QS-B and exhibits a smoother transition between the elastic and inelastic range with a more gradual change in stiffness. HS-B3 applied a positive peak in the opposite direction with no evident strength degradation between the two peaks of -3% . The continued loading in HS-B4 exhibits a closer behavior with the QS-B envelope in terms of strength degradation with both being loaded with the same axial load. However, the level of strength degradation is more substantial in the QS-B test, with a 33.8% strength reduction at the last cycle.



FIGURE 20 | Sequence in beam lateral buckling: (A) HS-A2; (B) HS-A3; and (C) HS-A4.

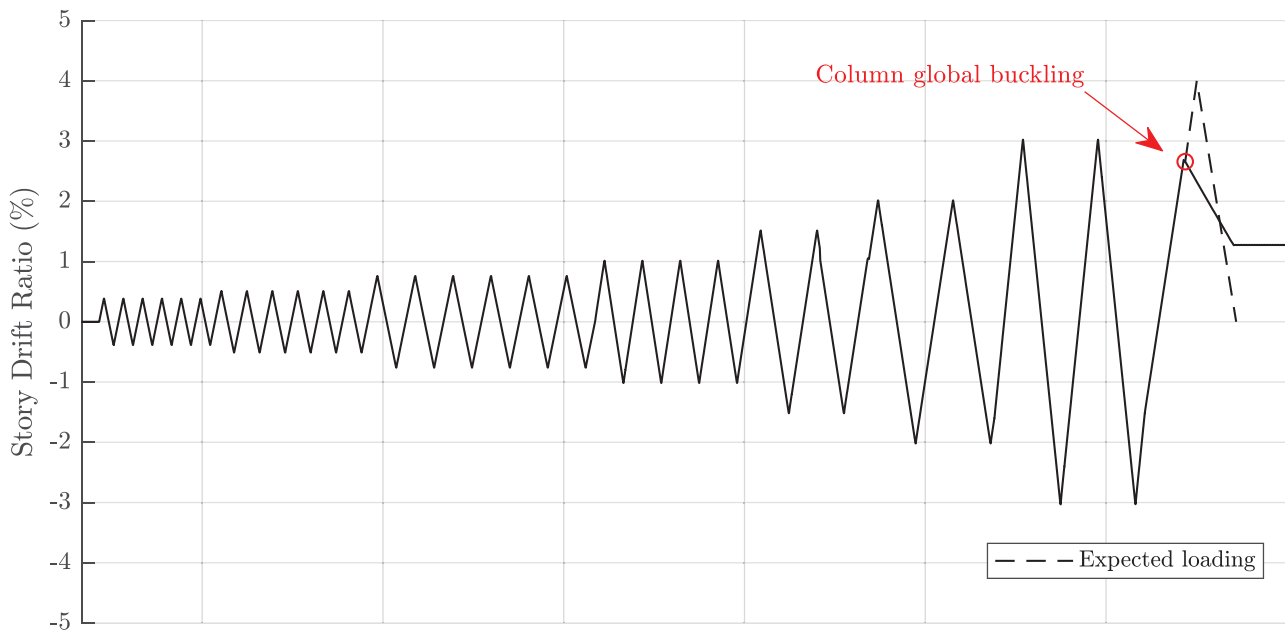


FIGURE 21 | Applied loading protocol for test QS-B.

This indicates the column did not exhibit highly ductile member behavior, consistent with the most updated edition of AISC 341–22 [21] (see Figure 2).

Figures 24 and 26 show photos of the column damage for QS-B and HS-B, respectively. After reaching a 2% drift ratio during QS-B, the first evidence of local buckling in the web was visually detected at the column base (Figure 24A). When the specimen was subjected to the first cycle at 3% drift, the severity of the buckling increased, exhibiting antisymmetric local buckling with a second local buckling wave coupled with lateral-torsional buck-

ling and out-of-plane global buckling, called coupled buckling [2]. Figure 24B,C shows the column coupled buckling at the end of QS-B. Although column buckling was more visually evident at 3% lateral deformation, drifting in the strain gauge measurements suggests it was triggered at 2% in QS-B (Figure 25A).

While HS-B2 produced the largest lateral deformation in the specimen, it did not produce observable buckling (Figure 26A). HS-B3 with increased axial load initiated the local buckling at the column base and HS-B4 increased the severity, with no observable global buckling. The loading beam began to tilt at the

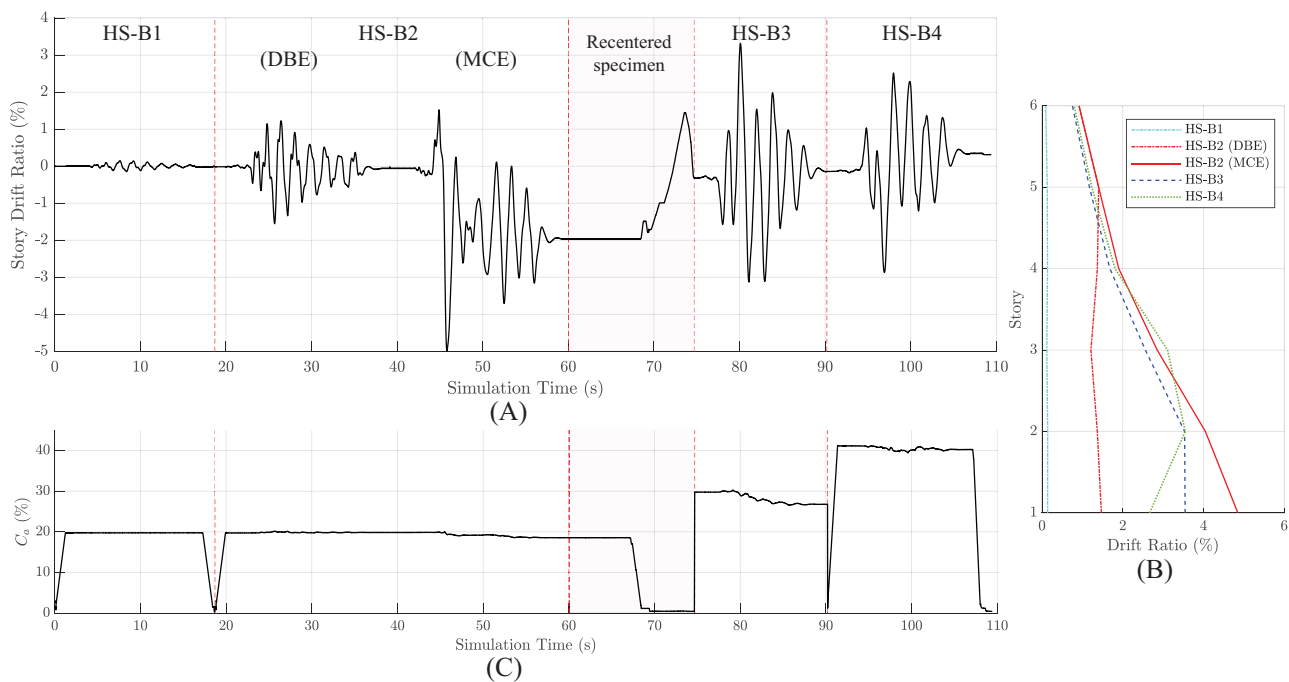


FIGURE 22 | Overall response from HS-B test sequence: (A) First story drift ratio; (B) maximum story drift ratio (numerical substructure); and (C) axial load history.

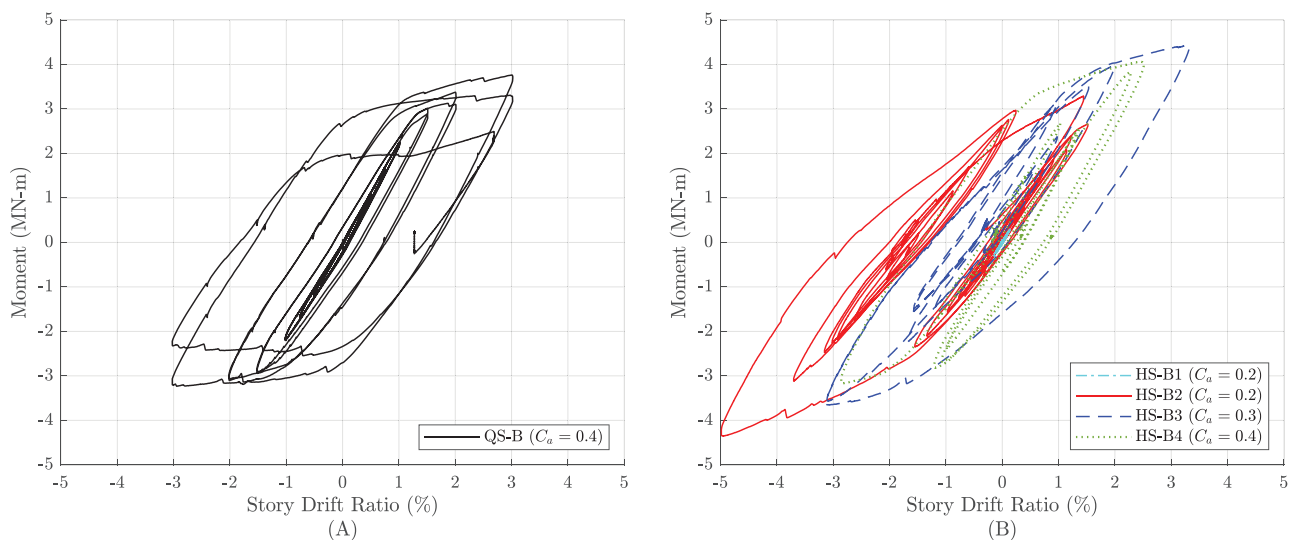


FIGURE 23 | Column base moment versus drift ratio: (A) QS-B and (B) HS-B.

end of HS-B4. After disassembling the specimen, an apparent out-of-plane bending can be observed (Figure 26D), suggesting out-of-plane global buckling also showed up during the hybrid tests. The strain distribution shows a limited deviation from the 45° line, indicating more symmetric behavior for HS-B2 (Figure 25B) and deviations indicating buckling during HS-B3.

A comparison of both tests shows that there was more damage during QS-B compared to HS-B. A direct comparison is not as straightforward for archetype A since the axial load of QS-B was higher than HS-B for most of the testing and a larger peak drift was achieved during HS-B. Nonetheless, QS-B and HS-B4 employed the same axial load and similar maximum lateral drift, exhibiting different final damage states. This indicates

that structural damage is not only related to the maximum deformation but also to cumulative damage.

Axial shortening for QS-B and HS-B is compared in Figure 27. Based on visual inspection and strain profile data mentioned above, buckling was not observed for drift ratios up to 1.5% for test QS-B. At that stage, axial shortening was composed of 5.3 mm due to the gravity loads, plus 3 mm after the last 1.5% drift cycle, completing a total Δ_{axial} of 8.3 mm. Upon concluding this test, Δ_{axial} was 94 mm at a maximum drift ratio of 3%.

HS-B2 test induced an initial gravity displacement of 3.6 mm in the specimen. Despite the large drift ratio produced by this

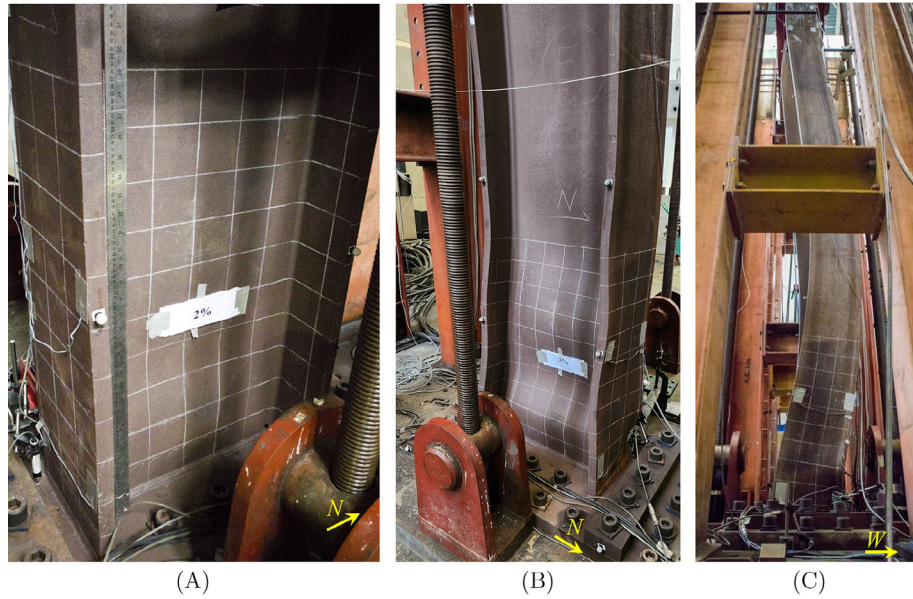


FIGURE 24 | Column base for QS-B: (A) After first 2% drift; (B) at the end of the test; and (C) lateral view at the end of the test.

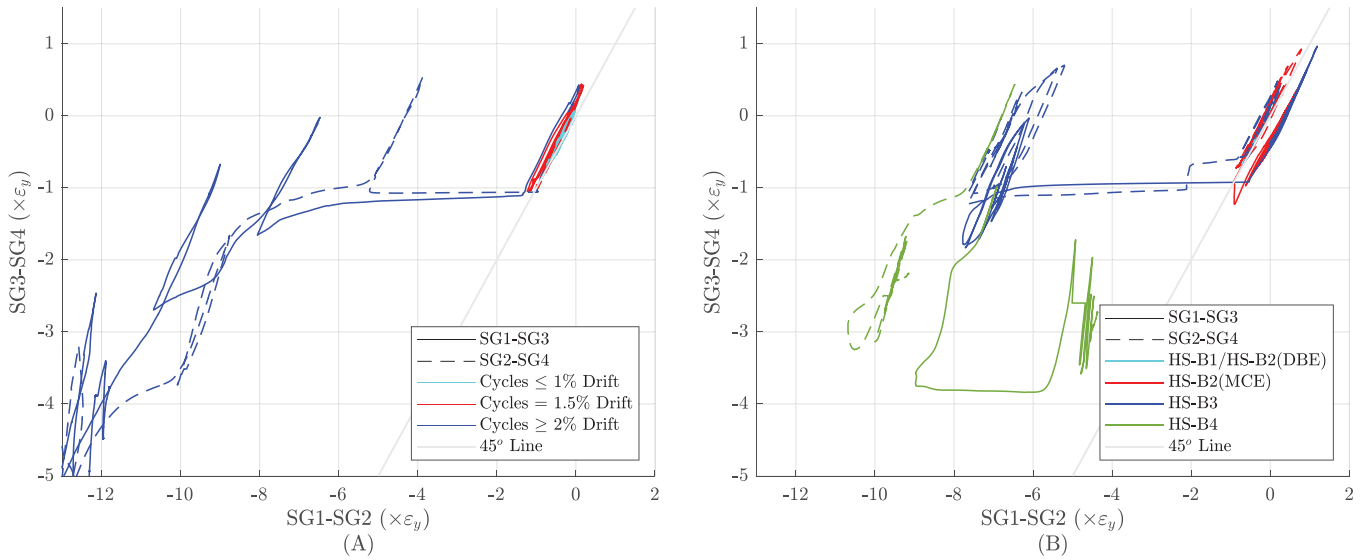


FIGURE 25 | Column flange strains at 65 cm from the base plate: (A) QS-B and (B) HS-B.

test, the total Δ_{axial} reached 8.2 mm, mainly due to steel yielding based on visual inspection and strain measurements. HS-B3 tests induced column buckling and a total shortening of 18.5 mm. Last, HS-B4 axial load matched QS-B, inducing $-2.9\%/2.5\%$ peak drifts and a total Δ_{axial} of 38.4 mm at the end of the test.

6.4 | Beam Response

The RBS response was also monitored during the testing of specimen B. During the QS-B test, the RBS exhibits smaller rotations and limited strength degradation (Figure 28A). This is consistent with the visual observations of limited local buckling as shown in Figure 29B. Unlike specimen A, no lateral buckling was observed during the QS protocol (Figure 29A). This might

be attributable to a combination of higher column torsional stiffness and out-of-plane beam stiffness. The largest RBS rotation occurred during test HS-B2, consistent with the drift level of the test, and maintains a stable response with no significant degradation in Figure 28B. No buckling was evidenced even at the end of HS-B4 (Figure 29C), highlighting the importance of cumulative inelastic deformation in the degrading behavior of the RBS connection. No fracture occurred in the beam flange CJP welds.

Consistent with the above observations, strain gauge measurements of Figure 30A indicate nonsymmetric beam behavior during QS-B starting at 2% drift. However, it is unclear if this resulted from minor local buckling in the RBS, lateral-torsional buckling of the beam, or a distortion resulting from the column buckling. For HS-B (Figure 30B), the pair of strain gauges show that the response remains mostly symmetric.

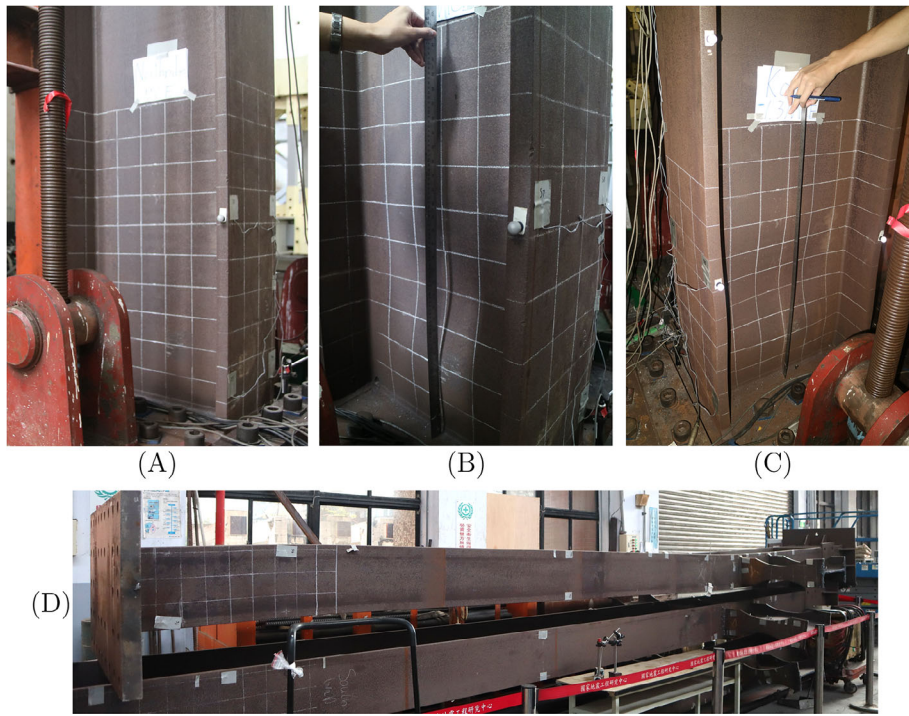


FIGURE 26 | Column base at the end of HS-B tests: (A) HS-B2; (B) HS-B3; (C) HS-B4; and (D) disassembled specimen column.

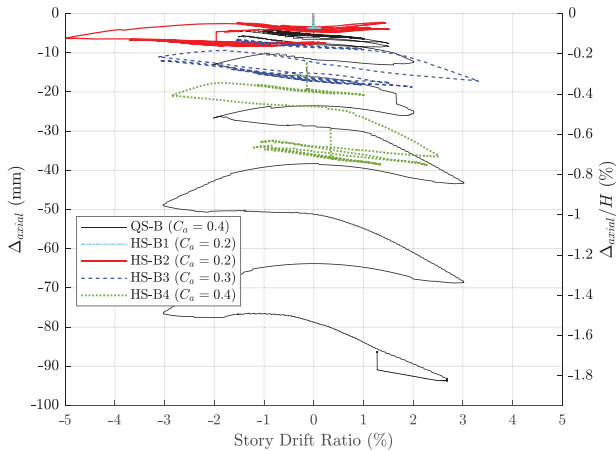


FIGURE 27 | Axial shortening versus column drift ratio for QS-B and HS-B.

7 | Subassembly Versus Member-Level Tests

The response of columns in the subassembly during QS tests presented here is compared with isolated column tests conducted at UC San Diego [11]. A series of columns were tested with different column sections, axial load levels, and boundary conditions to investigate the effect of these parameters. All columns were 18 ft in length, having the same height as in this study. Test ID “2L” corresponded to a W24 × 131 column section, with both ends fixed and constant axial load equivalent to $C_a = 0.16$ using Equation (1), corresponding to the same cross-section and similar axial load level as QS-A. Test ID “11M” corresponds to a W24 × 176 column section with both ends fixed and axial load equivalent to $C_a = 0.33$, same cross-section and similar axial load of test QS-B.

A comparison of the column behavior between member-level and subassembly-level test are presented below.

7.1 | Column Section W24 × 131 (Specimen A)

Member-level testing indicated that web and flange local buckling initiated at 3% drift and continued to increase in amplitude until 4% drift. These findings are consistent with the behavior noted during test QS-A. The antisymmetric local buckling mode was also the same for both specimens as shown in Figure 31.

The moment responses for both tests exhibit a comparable envelope and level of degradation initiated at around 3% drift (see Figure 32A). Member level test shows a larger initial stiffness due to the fixed-fixed boundary condition, which triggers column yielding at lower lateral deformations. However, once the column yields, member and subassembly specimens provide a similar moment response. This pattern was also identified by Chou et al. [12]. Figure 32B compares the axial shortening for both tests. Note that for the isolated column test, only half of the shortening is considered since the fixed-fixed boundary condition produces two-column ends with buckling. In contrast, for the subassembly test, the damage is concentrated at the fixed base. Comparable Δ_{axial} values are also evidenced for both tests, with reasonable variations considering the different loading conditions. These observations are consistent with Elkady et al. [10] when considering the boundary conditions effect.

7.2 | Column Section W24 × 176 (Specimen B)

For the W24 × 176 member level test, coupled buckling with the same pattern observed in the QS-B subassembly test was

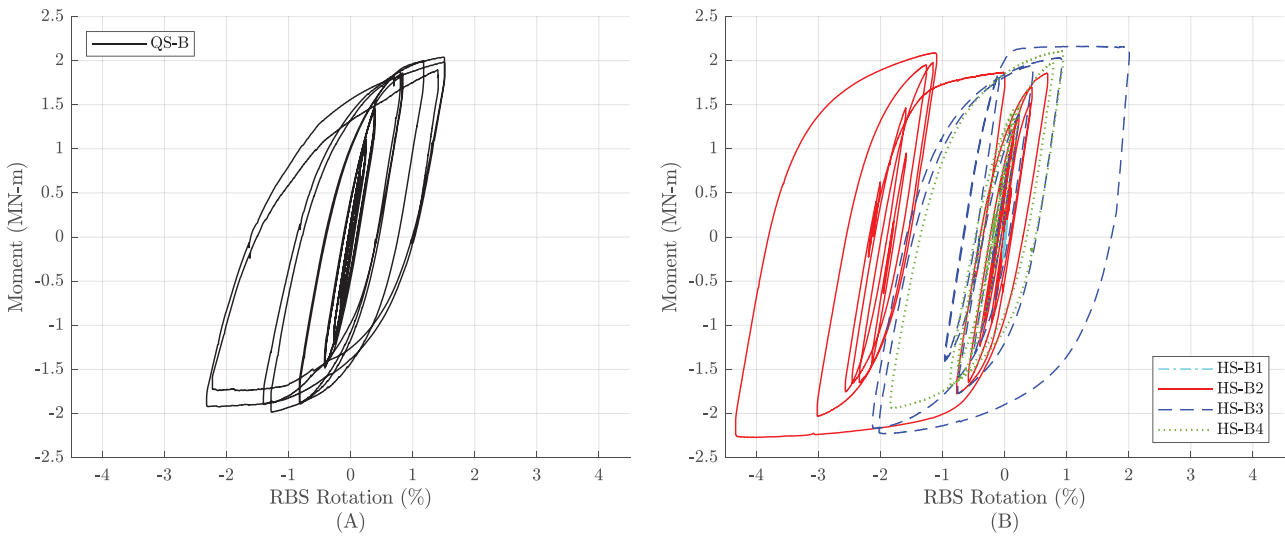


FIGURE 28 | RBS local moment-rotation response: (A) QS-B and (B) HS-B.

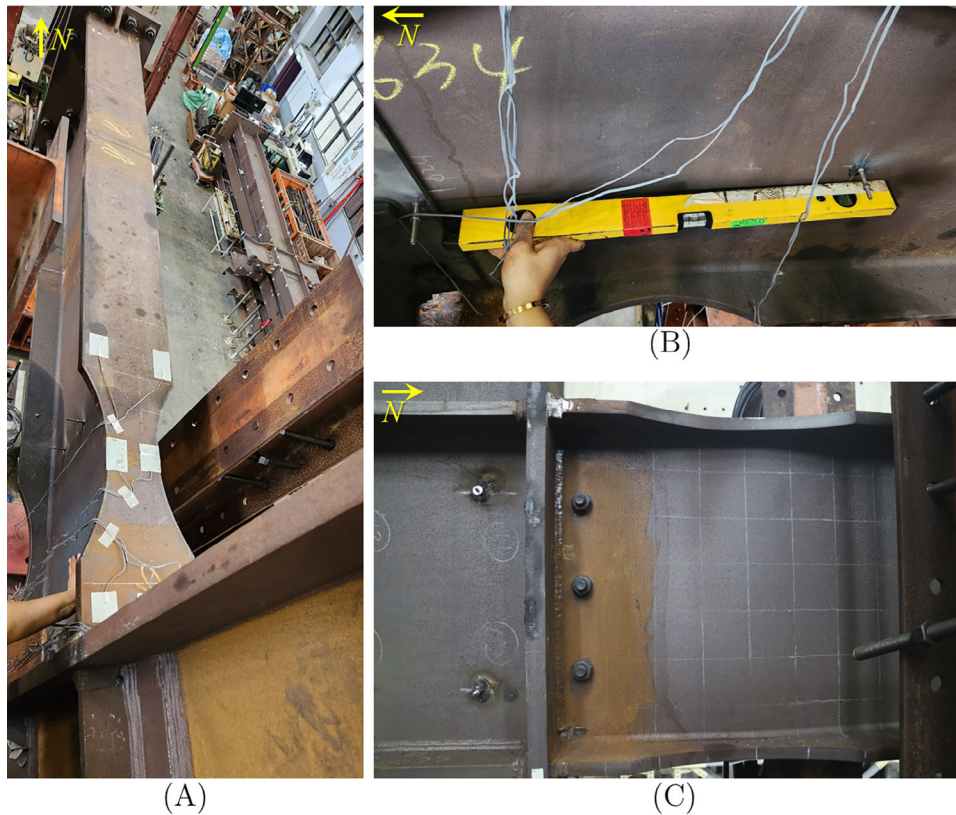


FIGURE 29 | Beams for specimen B: (A) Top view of the beam at the end of QS-B; (B) RBS at the end of QS-B; and (C) RBS at the end of HS-B4.

observed. During the member-level test, minor lateral-torsional buckling initiated at 1.5% drift and became more noticeable at 2% drift. This is in agreement with visual inspections and strain gauge measurements in QS-B. Figure 33 illustrates a comparison between both member-level and subassembly-level tests for 2% and 3% drift ratios. While the column moment versus drift ratio response (Figure 34A) from both tests show similar envelopes and levels of degradation, it is important to note that the subassembly test was conducted under a slightly larger axial load. The effect of boundary conditions on the initial stiffness is also evident in

these tests. Axial shortening (Figure 34B) is also almost identical in these two tests having a closer loading history in terms of drifts and applied axial loads.

8 | Conclusions

A series of quasi-static (QS) and hybrid simulations (HS) tests of four full-scale beam-to-column subassemblies were performed to study the seismic behavior of steel moment frames with deep

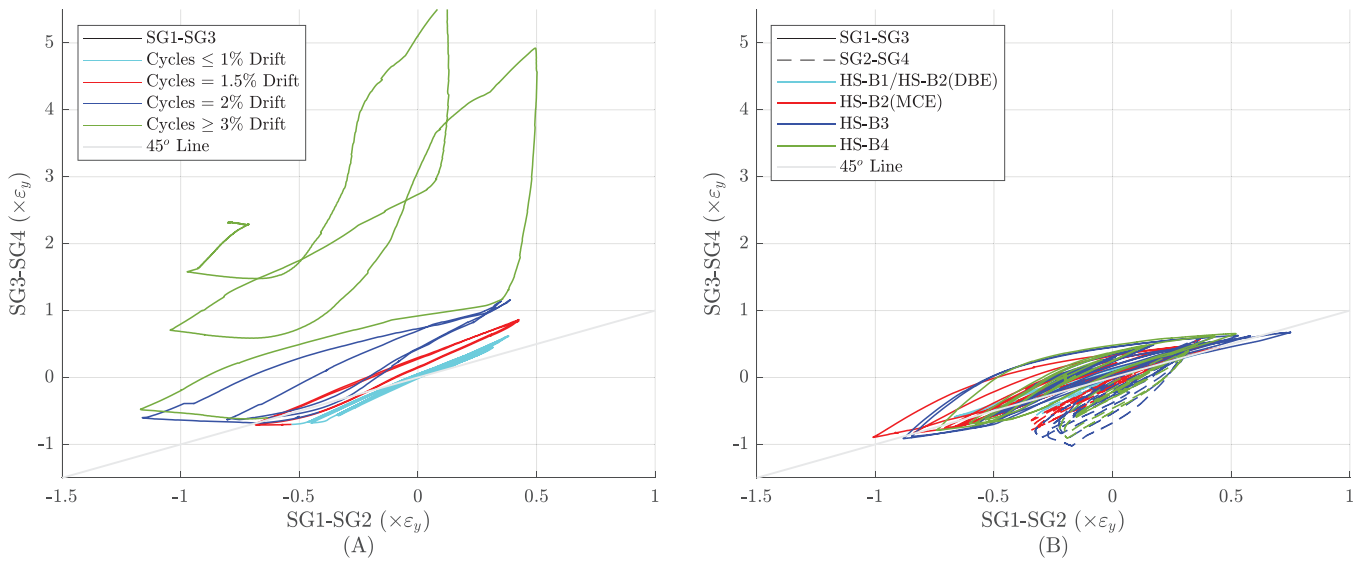


FIGURE 30 | Beam flange strains at 66 cm from the column face: (A) QS-B and (B) HS-B.

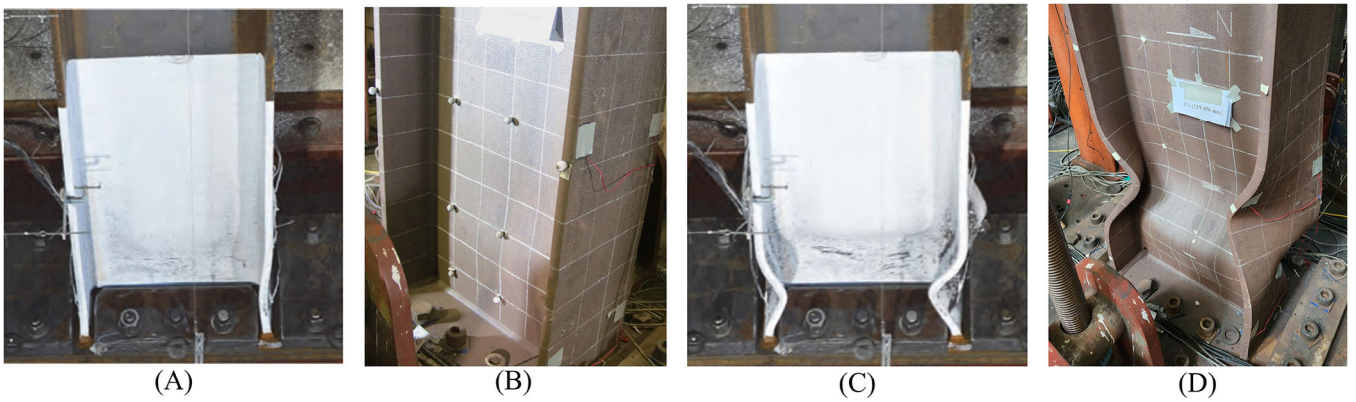


FIGURE 31 | W24 \times 131 column: (A) Column test at 3% drift; (B) subassembly test at 3.25% drift; (C) column test at 4% drift; and (D) subassembly test at 4.3% drift.

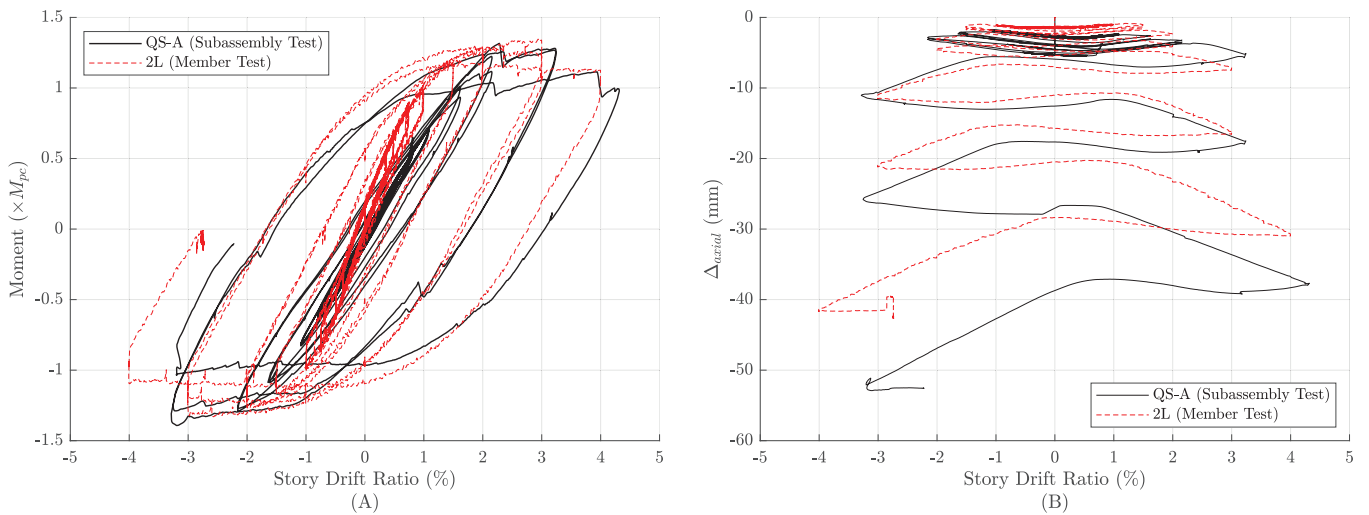


FIGURE 32 | W24 \times 131 column: (A) Moment versus drift and (B) axial shortening versus drift.

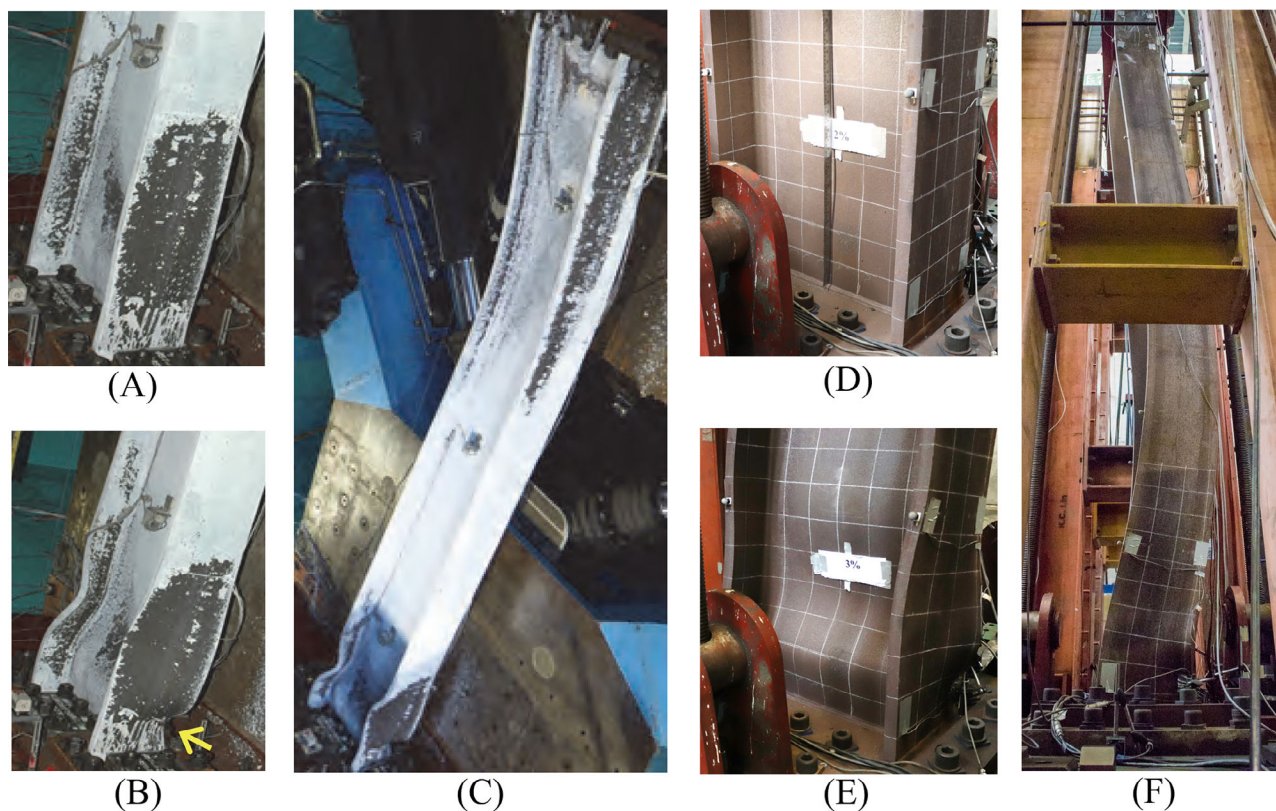


FIGURE 33 | Section W24 × 176: (A) Column test at 2% drift; (B) column test at 3% drift; (C) column test at 3% drift (lateral view); (D) subassembly test at 2% drift; (E) subassembly test at 3% drift; and (F) subassembly test at 3% drift (lateral view).

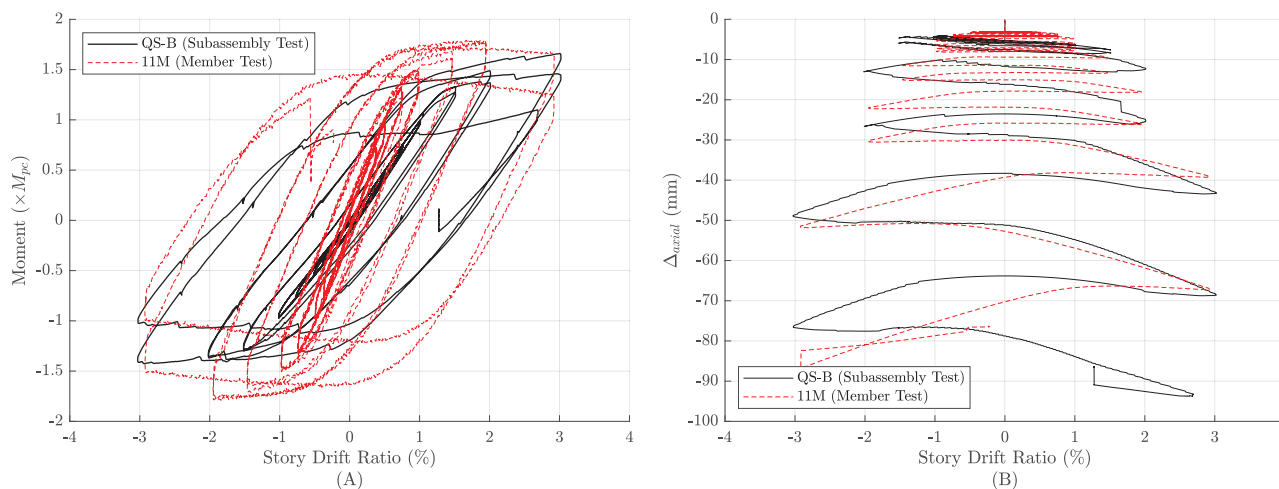


FIGURE 34 | Section W24 × 176: (A) Moment versus drift and (B) axial shortening versus drift.

and slender column sections. This study complements previous experimental studies conducted on isolated column members. The testing was conducted on two different column sections: W24 × 131 and W24 × 176, each paired with beams following code compliant-design. Two identical specimens of each type were tested with the one subjected to a QS loading protocol and the other subjected to HS that included a sequence for four ground motions ranging from DBE to MCE. The main findings are summarized below.

- Quasi-static protocols were shown to result in more damage for beams and columns compared to the loading history imposed by historical ground motions using HS to similar drifts. Specifically, strength degradation, buckling severity, and column shortening are the observed measurements impacted by the loading history. This suggests that damage induced by symmetric quasi-static protocols is a conservative estimate of the expected damage during earthquake-induced loads for the same maximum lateral deformation.

- The lower torsional stiffness of the column for specimen A and the tendency of the RBS to experience local and lateral-torsional buckling led to increased instabilities at the beam-column connection. This was also the case for the HS, when the column did not show significant buckling but had induced torsion by RBS buckling. This behavior should be further evaluated considering the constraints imposed by the presence of the diaphragm not included in this study.
- Specimen B with lower slenderness showed a more stable behavior based on column and RBS response as expected. However, if the column is subjected to moderate to high axial loads, the column may not be able to sustain large deformations before experiencing local and global buckling based on the QS test.
- Column axial shortening observed during HS is likely more related to steel yielding than column buckling when axial loads up to $C_a = 0.2$ are applied. In contrast, when the specimens were subjected to either a QS loading pattern or axial loads greater than $C_a = 0.2$ for QS or HS, column buckling became the dominant source of axial shortening. Around 90% of the total axial shortening for QS-A and QS-B is buckling-related, and 80% for HS-B.
- The highly ductile limit (λ_{hd}) for the web of I-shaped columns in Special Moment Frames is more stringent in AISC 341–22 [21] than that in AISC 341–16 [20]. Although the column for specimen QS-A met the AISC 341-16 compactness requirement by a large margin, it barely met the AISC 341-22 requirement. Therefore, it is not unexpected to see buckling of the column in this test.
- The experimental data from this study demonstrates that as the axial force level in columns increases, the point of maximum strength occurs at significantly lower drift angles than 0.04 radian. Furthermore, the rate of strength degradation increases substantially with higher axial loads. These observations provide empirical support for the new λ_{hd} limits in AISC 341-22. The findings underscore the importance of considering axial load effects on column performance.
- The buckling mode of specimen A was antisymmetric local buckling, while for specimen B it was coupled buckling, that is, a combination of local buckling and out-of-plane lateral-torsional buckling. This trend is in agreement with the observation of isolated columns and expected behavior as proposed by Ozkula and Uang [2].
- Experimental observations of isolated column tests agree well with those obtained from QS subassembly tests conducted in this study. Among the most important similarities are the overall column buckling modes depending on the column section, moment response envelope, level of axial shortening, and the level of deformation that triggers strength degradation and column buckling.
- Previous studies found that strength degradation and buckling occur slightly earlier in member-level column tests when the same axial load is used [12]. In this study, a slightly larger axial load in subassembly tests resulted in strength degradation and buckling occurring at the same deformation, making the comparison consistent.

This paper provides an overview of the testing program and highlights experimental observations on the behavior of the deep columns. The tests conducted provide a valuable dataset on full-scale testing of SMF subassemblies that is being made publicly available in DesignSafe [33, 34]. This data can support additional studies on the development of numerical models for both deep columns and beams with RBS.

Acknowledgments

This project was funded by NIST under Award 70NANB171TZ91 to the University of Michigan and UC San Diego and by the National Center for Research on Earthquake Engineering (NCREE) supported by the Ministry of Science and Technology (MOST 110-2625-M-002-015), Taiwan. The support of Andreas Schellenberg, M. Javad Hashemi, and the technical team of NCREE in implementing the hybrid testing is gratefully acknowledged.

Data Availability Statement

The data that support the findings of this study are openly available in DesignSafe Data Depot at <https://doi.org/10.17603/ds2-t1ry-4s93>, reference number PRJ-4820.

References

1. ASCE, ASCE/SEI 7–16 Minimum Design Loads and Associated Criteria for Buildings and Other Structures (American Society of Civil Engineers, 2016).
2. G. Ozkula and C. M. Uang, “Classification and Identification of Buckling Modes of Steel Columns Under Cyclic Loading,” *Journal of Structural Engineering* 149, no. 8 (2023): 04023097, <https://doi.org/10.1061/JSENDH.STENG-12156>.
3. A. Elkady and D. G. Lignos, “Analytical Investigation of the Cyclic Behavior and Plastic Hinge Formation in Deep Wide-Flange Steel Beam-Columns,” *Bulletin of Earthquake Engineering* 13 (2015): 1097–1118, <https://doi.org/10.1007/s10518-014-9640-y>.
4. G. Ozkula, Seismic Behavior, Modeling, and Design of Deep Wide-Flange Steel Columns for Special Moment Frames (University of California San Diego, 2017), <https://escholarship.org/uc/item/0gc7z55w>.
5. A. Elkady, G. Güell, and D. G. Lignos, “Proposed Methodology for Building-Specific Earthquake Loss Assessment Including Column Residual Axial Shortening,” *Earthquake Engineering & Structural Dynamics* 49, no. 4 (2020): 339–355, <https://doi.org/10.1002/EQE.3242>.
6. A. Islam and A. Imanpour, “Stability of Wide-Flange Columns in Steel Moment-Resisting Frames: Evaluation of the Canadian Seismic Design Requirements,” *Bulletin of Earthquake Engineering* 20 (2022): 1591–1617, <https://doi.org/10.1007/s10518-021-01313-8>.
7. C. D. Stoakes and L. A. Fahnestock, “Strong-Axis Stability of Wide Flange Steel Columns in the Presence of Weak-Axis Flexure,” *Journal of Structural Engineering* 142, no. 5 (2016): 04016004, [https://doi.org/10.1061/\(ASCE\)ST.1943-541X.0001448](https://doi.org/10.1061/(ASCE)ST.1943-541X.0001448).
8. J. Fogarty, T. Y. Wu, and S. El-Tawil, “Collapse Response and Design of Deep Steel Columns Subjected to Lateral Displacement,” *Journal of Structural Engineering* 143, no. 9 (2017): 04017130, [https://doi.org/10.1061/\(ASCE\)ST.1943-541X.0001848](https://doi.org/10.1061/(ASCE)ST.1943-541X.0001848).
9. G. Ozkula, C. M. Uang, and J. Harris, “Development of Enhanced Seismic Compactness Requirements for Webs in Wide-Flange Steel Columns,” *Journal of Structural Engineering* 147, no. 7 (2021): 04021100, [https://doi.org/10.1061/\(ASCE\)ST.1943-541X.0003036](https://doi.org/10.1061/(ASCE)ST.1943-541X.0003036).
10. A. Elkady and D. G. Lignos, “Full-Scale Testing of Deep Wide-Flange Steel Columns Under Multiaxial Cyclic Loading: Loading Sequence,

Boundary Effects, and Lateral Stability Bracing Force Demands,” *Journal of Structural Engineering* 144, no. 2 (2017): 04017189, [https://doi.org/10.1061/\(ASCE\)ST.1943-541X.0001937](https://doi.org/10.1061/(ASCE)ST.1943-541X.0001937).

11. P. Chansuk, G. Ozkula, C. M. Uang, and J. L. Harris, Seismic Behavior and Design of Deep, Slender Wide-Flange Structural Steel Beam-Columns, Technical Note (NIST TN), National Institute of Standards and Technology, Gaithersburg, MD, (2021), <https://doi.org/10.6028/NIST.TN.2169>.

12. C. Chou, Y. Lai, H. Xiong, et al., “Effect of Boundary Condition on the Cyclic Response of I-Shaped Steel Columns: Two-Story Subassembly Versus Isolated Column Tests,” *Earthquake Engineering & Structural Dynamics* 51, no. 14 (2022): 3434–3455, <https://doi.org/10.1002/EQE.3730>.

13. T. Y. Wu, S. El-Tawil, and J. McCormick, “Seismic Collapse Response of Steel Moment Frames With Deep Columns,” *Journal of Structural Engineering* 144, no. 9 (2018): 04018145, [https://doi.org/10.1061/\(ASCE\)ST.1943-541X.0002150](https://doi.org/10.1061/(ASCE)ST.1943-541X.0002150).

14. A. Islam and A. Imanpour, “Seismic Stability of Steel Wide-Flange Columns in Ductile Moment-Resisting Frames: Out-of-Plane Response and Design Recommendations,” *Bulletin of Earthquake Engineering* 21, no. 7 (2023): 3493–3519, <https://doi.org/10.1007/S10518-023-01653-7/FIGURES/12>.

15. G. A. MacRae, C. R. Urmson, W. R. Walpole, P. Moss, K. Hyde, and C. Clifton, “Axial Shortening of Steel Columns in Buildings Subjected to Earthquakes,” *Bulletin of the New Zealand Society for Earthquake Engineering* 42, no. 4 (2009): 275–287, <https://doi.org/10.5459/bnzsee.42.4.275-287>.

16. K. Wang, C. Chou, C. Huang, et al., “Hybrid Simulation of a Steel Dual System With Buckling-Induced First-Story Column Shortening: A Mixed Control Mode Approach,” *Earthquake Engineering & Structural Dynamics* 52, no. 12 (2023): 3727–3745, <https://doi.org/10.1002/EQE.3944>.

17. AISC, ANSI/AISC 360-16 Specification for Structural Steel Buildings (American Institute of Steel Construction, 2016).

18. C. Sepulveda, G. Mosqueda, K. J. Wang, et al., “Hybrid Simulation Framework With Mixed Displacement and Force Control for Fully Compatible Displacements,” *Earthquake Engineering & Structural Dynamics* 53, no. 2 (2024): 838–855, <https://doi.org/10.1002/eqe.4048>.

19. C. Sepulveda, M. Cheng, T. Becker, et al., “Selective Online Model Updating in Hybrid Simulation of a Full-Scale Steel Moment Frame,” *Earthquake Engineering & Structural Dynamics* 53, no. 10 (2024): 3071–3092, <https://doi.org/10.1002/eqe.4149>.

20. AISC, ANSI/AISC 341-16 Seismic Provisions for Steel Structural Buildings (American Institute of Steel Construction, 2016).

21. AISC, ANSI/AISC 341-22 Seismic Provisions for Steel Structural Buildings (American Institute of Steel Construction, 2022).

22. AISC, ANSI/AISC 358-16 Prequalified Connections for Special and Intermediate Steel Moment Frames for Seismic Applications (American Institute of Steel Construction, 2016).

23. F. McKenna, M. H. Scott, and G. L. Fenves, “Nonlinear Finite-Element Analysis Software Architecture Using Object Composition,” *Journal of Computing in Civil Engineering* 24, no. 1 (2009): 95–107, [https://doi.org/10.1061/\(ASCE\)CP.1943-5487.0000002](https://doi.org/10.1061/(ASCE)CP.1943-5487.0000002).

24. A. Gupta and H. Krawinkler, *Seismic Demands For Performance Evaluation Of Steel Moment Resisting Frame Structures*, Blume Earthquake Engineering Center, 1999, accessed October 27, 2021, <http://blume.stanford.edu>.

25. L. F. Ibarra, R. A. Medina, and H. Krawinkler, “Hysteretic Models That Incorporate Strength and Stiffness Deterioration,” *Earthquake Engineering & Structural Dynamics* 34, no. 12 (2005): 1489–1511, <https://doi.org/10.1002/EQE.495>.

26. D. G. Lignos and H. Krawinkler, “Deterioration Modeling of Steel Components in Support of Collapse Prediction of Steel Moment Frames Under Earthquake Loading,” *Journal of Structural Engineering* 137, no. 11 (2011): 1291–1302, [https://doi.org/10.1061/\(ASCE\)ST.1943-541X.0000376](https://doi.org/10.1061/(ASCE)ST.1943-541X.0000376).

27. C. Sepulveda, G. Mosqueda, C. Uang, C. C. Chou, and K. J. Wang, “Hybrid Simulation Using Mixed Displacement and Equivalent-Force Control to Capture Column Shortening in Frame Structures,” in *12th National Conference on Earthquake Engineering* (NCEE, 2022).

28. M. J. Hashemi and G. Mosqueda, “Innovative Substructuring Technique for Hybrid Simulation of Multistory Buildings Through Collapse,” *Earthquake Engineering & Structural Dynamics* 43, no. 14 (2014): 2059–2074, <https://doi.org/10.1002/eqe.2427>.

29. A. Krawinkler, R. Gupta, R. Medina, and N. Luco, “Development of Loading Histories for Testing of Steel Beam-to-Column Assemblies,” Technical Report, SAC Steel Project, Stanford University, (2000).

30. G. MacRae, “The Seismic Response of Steel Frames” (PhD thesis, University of Canterbury, 1989).

31. A. Elkady and D. G. Lignos, “Improved Seismic Design and Nonlinear Modeling Recommendations for Wide-Flange Steel Columns,” *Journal of Structural Engineering* 144, no. 9 (2018): 04018162, [https://doi.org/10.1061/\(ASCE\)ST.1943-541X.0002166](https://doi.org/10.1061/(ASCE)ST.1943-541X.0002166).

32. G. Ozkula, J. L. Harris, and C. M. Uang, “Buckling-Induced Shortening of Deep W-Shape Columns in Seismic Steel Frames,” in *11th U.S. National Conference on Earthquake Engineering*, 2018.

33. C. Sepulveda and G. Mosqueda, “Hybrid Simulation and Quasistatic Test—Prototype A,” DesignSafe-CI, Data Project PRJ-4820: Hybrid and Cyclic Testing of Steel Moment Frames with Deep Column, (2024), <https://doi.org/10.17603/DS2-TIRY-4S93>.

34. C. Sepulveda and G. Mosqueda, “Hybrid Simulation and Quasistatic Test—Prototype B,” DesignSafe-CI, Data Project PRJ-4820: Hybrid and Cyclic Testing of Steel Moment Frames with Deep Column, (2024), <https://doi.org/10.17603/ds2-r1eb-b761>.

APPENDIX

A set of 30 ground motions was initially selected and scaled using the conditional spectrum method with a conditioning period of 1.4 s based on the value used for the frame design. A subset of these motions was then chosen for use in the hybrid simulations. The response spectrum of the ground motions used during testing are shown on Figure A1.

Table A1 presents the individual measured properties obtained from the coupon tests normalized by their nominal values if any. Some values in the table are missing because it was not possible to obtain samples from certain areas of specific members.

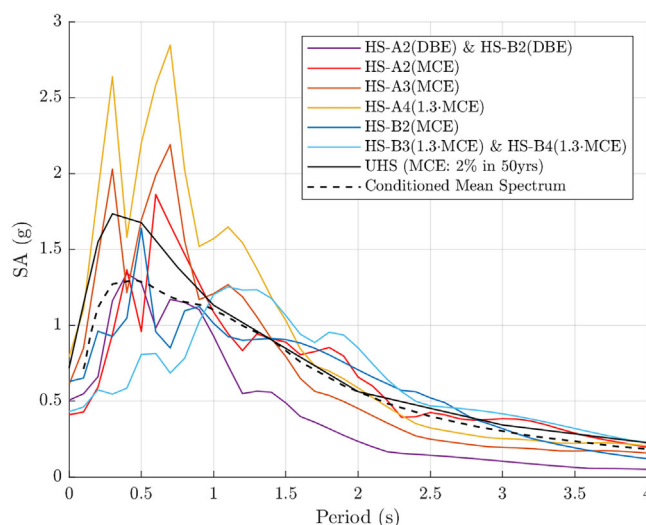


FIGURE A1 | Response spectrum of ground motion records used on hybrid simulations.

TABLE A1 | Normalized material properties from coupon testing.

Label	Location	Yield stress (345 MPa)	Ultimate stress (450 MPa)	Young's modulus (200 GPa)	Strain at F_u (%)	Fracture elongation (%)
Q-A	Column web	—	—	—	—	—
	Column flange	1.16	1.20	1.02	16.1	29.6
	Beam web	1.33	1.28	1.00	11.8	19.6
	Beam flange	1.16	1.15	0.97	16.5	27.2
HS-A	Column web	1.35	1.35	1.19	12.8	24.0
	Column flange	1.36	1.41	1.32	17.4	28.8
	Beam web	1.37	1.32	1.01	11.4	19.8
	Beam flange	1.14	1.15	1.05	15.8	27.4
Q-B	Column web	1.28	1.26	1.01	14.2	25.3
	Column flange	1.17	1.24	0.96	15.2	29.2
	Beam web	—	—	—	—	—
	Beam flange	—	—	—	—	—
HS-B	Column web	1.19	1.24	1.17	13.7	24.1
	Column flange	1.20	1.23	1.02	15.1	28.0
	Beam web	1.19	1.16	1.00	12.7	24.1
	Beam flange	1.11	1.18	1.13	13.8	28.6
Average		1.23	1.24	1.06	14.3	25.8
Standard deviation		0.0932	0.0792	0.105	1.86	3.37